Research Square

Preprints are preliminary reports that have not undergone peer review.
They should not be considered conclusive, used to inform clinical practice,
or referenced by the media as validated information.

CoZnFeO4 Prepared by Waste Ferrous Sulfate as Iron Source: Synthesis, Characterization and Photocatalytic Degradation of Methylene Blue

Pan Zhang
Sichuan University
Yirui Shu
Sichuan University
Yanjun Zhong
Sichuan University
Lin Yang (18980632893@163.com)
Sichuan University https://orcid.org/0000-0002-8709-1712
Xiushan Yang
Sichuan University

Research Article

Keywords: Ferrite, Solid waste utilization, Wastewater degradation, Photocatalytic

Posted Date: March 18th, 2021

DOI: https://doi.org/10.21203/rs.3.rs-309649/v1

License: This work is licensed under a Creative Commons Attribution 4.0 International License.
Read Full License

Version of Record: A version of this preprint was published at Journal of Materials Science: Materials in Electronics on July 29th, 2021. See the published version at https://doi.org/10.1007/s10854-021-06562-6.

$CoZnFeO_4$ prepared by waste ferrous sulfate as iron source: Synthesis, characterization and photocatalytic degradation of methylene blue

Pan Zhang[1,2], Yirui Shu[1,2], Yanjun Zhong[1,2], Lin Yang[1,2*],Xiushan Yang[1,2*]

Abstract: Aiming at devloping novel low cost and high performance catalyst for degradation of methylene blue in industrial waste water. Waste ferrous sulfater which is a industrial waste produced in the process of producing titanium dioxide, $CoZnFeO_4$ is synthesized from waste ferrous sulfate by solid phase method. The experimental results show that $CoZnFeO_4$ has better catalytic performance than other control samplesc: the degradation rate of methylene blue reaches 100% within 8 min, which maintains high catalytic activity after 5 cycles. Zeta potential and ICP-MS tests show that the degradation reaction occurs in the catalyst. The degradation pathway of methylene blue is verified by ESI-MS. These findings provide a low cost and simple strategy for rational design and modulation of catalysts for the industrial degradation of organic pollutants. It not only realizes the use of waste to treat waste, but also

1. Chemical Science and Engineering College, Sichuan University, Chengdu 610065, China, P R

2. Engineering Research Center of Comprehensive Utilization and Clean Processing of Phosphorus，Chengdu 610065, China, P R

* **Corresponding author**: Lin Yang; TEL: +862885405201; E-mail:18980632893@163.com

* **Corresponding author**: Xiu-shan Yang; TEL: +862885405201; E-mail:370216649@qq.com

1. Chemical Science and Engineering College, Sichuan University, Chengdu 610065, China, P R

2. Engineering Research Center of Comprehensive Utilization and Clean Processing of Phosphorus，Chengdu 610065, China, P R

accords with the current concept of green chemistry.

Keywords: Ferrite; Solid waste utilization; Wastewater degradation; Photocatalytic

1. Introduction

At present, the global annual output of dyestuff exceeds 7 million tons, and –the dyestuff varieties of dyestuff have more than 100,000 kinds. Nearly 15% of dyestuff is discharged into wastewater every year. Organic dyestuff wastewater has become an urgent problem to be solved in all countries [1]. Most organic dyes are in the form of aromatic groups such as benzene, naphthalene, anthracene, and quinone, which are highly mutagenic and carcinogenic and pose a growing threat to the water environment [2,3]. Among them, methylene blue (MB) is one of the most common dye, but it is difficult to be degraded by some conventional methods, easy to cause serious environmental pollution.

At present, the treatment of organic dye wastewater including MB dye wastewater mainly includes advanced oxidation method [4], precipitation, ion exchange, flocculation, a biological method [5], and membrane filtration [81]. In the advanced oxidation method, photocatalysis is a cheap and efficient method, which efficiently convert solar energy into chemical energy, which is one of the most ideal strategies to solve environmental pollution [6]. In 1972, the report of using TiO_2 electrodes to achieve photochemical decomposition of water to produce H_2 aroused the interest and exploration of a large number of scholars [7]. Since then, a series of systems (such as TiO_2, ZnO, ZnS) semiconductor photocatalysts have been reported

to decolorize organic pollutants and harmful microorganisms. However, due to the large bandgap width of these semiconductor photocatalysts, they can only use the ultraviolet region (only 4% of the solar energy), which seriously hinders the full utilization of solar energy resources. So, to make more efficient use of the visible light region (> 400 nm), it's important to use a visible-light-induced photocatalyst that improves recycling efficiency.

As a kind of important magnetic material, $ZnFe_2O_4$ has been the subject of intense research for potential application in the recovery of photocatalysts, magnetic resonance imaging, and high-density storage. Spinel zinc ferrite has a narrow bandgap (2.11 eV), high sensitivity to visible light, photochemical stability, and low toxicity, and is expected to be a visible light catalytic catalyst [36]. However, due to its wide bandgap and poor electron and hole separation ability, its photocatalytic activity is still a difficult problem. Therefore, to improve the ability of charge transfer, it is necessary to modify pure zinc ferrite materials. However, the catalytic activity of spinel ferrite depends entirely on octahedral position, so its catalytic activity is directly related to the cation on octahedron. Studies have shown that cobalt ions can occupy the position of ferrite octahedron. Sanadi et al. doped Co with $ZnAlCrO_4$ for photocatalytic decolorization of Rhodamine B (Rhb), and the results showed that the decolorization rate of Rhb increased from 57% to 83% after doping Co, indicating that cobalt ions can improve charge transfer, which is of great significance for photocatalysis[8].

Waste ferrous sulfate is an industrial by-product produced during the production of titanium dioxide by a sulphuric acid method. In 2018, the titanium dioxide industry produced more than 7 million tons of ferrous sulfate as a by-product [10]. With the increasing demand for titanium dioxide, the annual growth rate of by-products is more than 10%, which seriously restricts the sustainable development of the titanium dioxide industry. At present, only a small part of waste ferrous sulfate is recycled and the rest is still disposed of as industrial waste solid [11,12]. Therefore, the accumulation of waste ferrous sulfate not only causes a huge waste of sulfur and iron resources but also causes serious environmental pollution. It has become an urgent task to explore the resource utilization of waste ferrous sulfate.

In this study, $CoZnFeO_4$ is prepared by a one-step solid-phase method with low cost, simple process, simple operation, and easy industrialization. To reduce the synthesis cost, $CoZnFeO_4$ nanoparticles are prepared with waste ferrous sulfate as an iron source and pyrite as a reducing agent, which are used as photocatalyst for decolorizing MB. The physical and chemical properties of $CoZnFeO_4$ are characterized by X-ray diffraction (XRD), field emission scanning electron microscopy (FESEM), Fourier transforms infrared spectroscopy (FT-IR), and X-ray electron energy spectroscopy (XPS). The optical properties are analyzed by UV-Vis diffuse reflectance spectroscopy (UV-Vis DRS) and fluorescence spectroscopy (PL). Zeta potentiometer measures the surface charge of nano ions under different pH conditions. Photocatalytic degradation pathways and possible degradation products are also discussed by ESI-MS. This study not only alleviates the pressure of

environmental pollution but also converts waste ferrous sulfate into resources, realizing waste control by waste.

2. Experimental Methods

2. 1. Materials

In this study, the waste ferrous sulfate ($FeSO_4$, Panzhihua Iron & Steel Group Co. LTD, China), which is the main byproduct of titanium dioxide prepared by the sulfuric acid method. The sample composition is shown in Table 1. The sample composition of pyrite (FeS_2, Sichuan Hanyuan Chemical Co. LTD, China) is shown in Table 2. Ferric oxide (Fe_3O_4), ferric oxide (Fe_2O_3), zinc oxide (ZnO), cobalt oxide (Co_3O_4), zinc sulfate ($ZnSO_4 \cdot 7H_2O$), methylene blue($C_{16}H_{18}ClN_3S \cdot 3H_2O$) (Chengdu Cologne Chemicals Co. LTD, China). Cobalt sulfate ($CoSO_4 \cdot 7H_2O$), hydrogen peroxide (H_2O_2), sodium hydroxide（NaOH), muriatic acid (HCl), benzoquinone (BQ), nitrate (KNO_3), potassium bicarbonate ($KHCO_3$), monopotassium phosphate (KH_2PO_4), potassium chloride (KCl) (Chengdu Jinshan Chemical Reagent Co. LTD, China). All solutions are prepared using deionized water.

Table 1 The chemical compositions of ferrous sulfate.

Compositions	Fe_2O_3	SO_2	MgO	ZnO	CaO	Al_2O_3	NiO
wt.%	52.10	45.55	2.10	0.19	0.01	0.012	0.013

Table 2 The main chemical compositions of pyrite in the experiment.

Compositions	Fe	S	Ca	Si	Pb	Al	Mn

wt.%	48.30	38.05	3.43	1.08	0.88	0.32	0.306

2.2. Preparation of $CoZnFeO_4$

$CoZnFeO_4$ is synthesized form using ferrous sulfate as the iron source and pyrite as the reducing agent, by solid-phase reduction under the condition of nitrogen. The reaction of synthetic $CoZnFeO_4$ is as follows:

$$3ZnSO_4 + 3CoSO_4 + 2FeSO_4 + FeS_2 \rightarrow 3CoZnFeO_4 + 10SO_2(g) \quad (1)$$

The experimental process of preparing $CoZnFeO_4$ is as follows: ferrous sulfate, pyrite, $ZnSO_4 \cdot 7H_2O$, and $CoSO_4 \cdot 7H_2O$ are dried for 120 min at 393.15 K respectively, and the samples are taken according to the molar ratio 4:4:3.5:1, 11.50 g $ZnSO_4 \cdot 7H_2O$, 11.24 g $CoSO_4 \cdot 7H_2O$, 9.73 g waste ferrous sulfate, and 1.20 g FeS_2 are weighed and mixed in a high-speed ball mill for 120 min. The mixture is put into a high-temperature zone of the tube furnace under nitrogen protected and heated to 823.15 K for 60 min. After natural cooling to room temperature, the impurities are wished with anhydrous ethanol and deionized water in turn. Finally, it is vacuum dried for 300 min at 372.15 K.

2.3. Degradation experiment of methylene blue

The decolorization rates of MB at different concentrations are studied, the effect of different nanomaterials on decolorizing Photo-Fenton reaction. A certain amount of $CoZnFeO_4$ nanoparticles are dispersed into MB solution as a catalyst, and then the given pH value of MB solution is adjusted using an automatic pH titrator (4 mol/L NaOH or 4 mol/L HCl). The dark chamber stirred for 1h to achieve the balance of

absorption and desorption. Then, the 5 mL of H_2O_2 at a certain concentration is added into the above-mixed solution and reacts under a certain wavelength for the light-ton reaction. The decolorization effect of MB under different reaction times is obtained under the parallel apparatuses. After taking out the parallel reaction solutions with different reaction times, 3.33 mL tert-butanol solution is added as the reaction inhibitor, the nanocatalyst is removed by centrifugation, and the concentration of MB in the supernatant is determined by spectrophotometer.

2.4. Characterization Method

The crystal structure of solid powder is analyzed by X-ray diffraction (XRD, Empyrean, PANalytical). Scanning electron microscope (SEM, JSM-5900LV) and X-ray microregion analysis (EDS, JSM-5900LV) is used to analyze the sample morphology and element composition. X-ray photoelectron spectroscopy (XPS, Kratos, XSAM800) is used to analyze the surface composition of the samples. The nitrogen adsorption technique (BET, Brunner-Emmet-Teller) is used to determine the specific surface area of the sample. The surface properties of the samples are recorded by Fourier infrared spectroscopy (FT-IR, Nicolet IS10) at wavelength range (4000-200 cm^{-1}). The optical properties of nanomaterials are analyzed by UV-Vis near-infrared spectrophotometer (Shimadzu, UV-3600) and fluorescence spectrometer (Hitachi, F-7000). Ethylene Diamine Tetraacetie Acid (EDTA), 1,4-Benzoquinone (BQ), Cupric cell ($Cu(NO_3)_2$) are used as free radical traps. The Zn, Fe, and Co ions released by the catalyst are detected by a plasma spectrometer (ICP-MS, Agilent 7700). Adjusting the pH of the solution using the automatic pH titrator (Metrohm, 916

144 Ti-Touch). The surface charge of nanoparticles is measured by Zetasizer Nano-ZS
145 under different pH conditions. ESI-MS spectra are obtained on Bruker Amazon SL
146 spectrometer (BrukerInc.Switzerland). Ion chromatography (Thermo Scientific,
147 ICS-600) is used to measure anions.

148 **3. Results and discussion**

149 **3.1 Characterization of nanomaterials**

150 Fig. 1a shows the XRD pattern of the synthesized $CoZnFeO_4$ nanoparticles. The
151 XRD located at 2θ =18.04°, 29.81°, 35.14°, 36.99°, 42.74°, 53.12°, 56.60°, 62.189°,
152 70.46°, 73.60°, 74.58°, and 78.57° diffraction angles, which corresponds to the crystal
153 surface of $[Fe^{3+}]_A[M^{2+}Fe^{3+}]BO_4$ (111), (220), (311), (222), (400), (422), (511), (440),
154 (620), (533), (622), (444) ($ZnFe_2O_4$: JCPDS Card No.79-1150 and $CoFe_2O_4$: JCPDS
155 Card No.22-1086), indicating that the formation of the $CoZnFeO_4$ nanoparticles are
156 composed of a single phase. It indicates that $CoZnFeO_4$ may be formed. According to
157 the famous Debye-Scherer equation [13], the average grain size of the synthesized
158 CMFNPs is estimated to be 27 nm. The infrared spectrum of the nanoparticle is
159 shown in Fig.1b. broadband at 3445 cm^{-1} and, 1632 cm^{-1} can be considered as the
160 stretching vibration of -OH. Besides, the absorption peak of 1376 cm^{-1} also indicates
161 the presence of a large amount of -OH. Moreover, the absorption peaks of 1074 cm^{-1}
162 indicate the existence H_2O deformation vibration. The strong characteristic bands
163 observed at 572 cm^{-1} can be attributed to the stretching vibration of M^{3+}-O^{2-}
164 octahedron of typical spinel ferrite, It also indicates that $CoZnFeO_4$ may be produced.
165 The surface composition and chemical state of the molded sample are determined by

X-ray photoelectric spectrometry, as shown in Fig. 2. The peaks of Fe, Co, Zn, and O are observed in Fig. 2a. In Fig. 2b, the two main peaks of the combined energy 780.3 eV and 795.2 eV belong to the core energy levels of Co $2p_{3/2}$and Co $2p_{1/2}$ [14,15], this indicates the existence of Co^{3+} in nanomaterials. In Fig.2c, the peaks of the binding energies of 711.2 eV and 724.63 eV belong to the core energy levels of Fe $2p_{3/2}$ and Fe $2p_{1/2}$ [16,17], this is typical of Fe (III) in inverse spinel ferrite. The synthesis of $CoZnFeO_4$ is demonstrated by XRD and FTIR. In Fig 2d, O1s spectrum is divided into absorption peaks of 530.15 eV, 531.69 eV, and 532.64 eV, corresponding to lattice oxygen (O^{2-}) in metal oxides, the hydroxyl group (-OH) is hydroxylated on the surface and physically adsorbed the water on the sample surface [18].

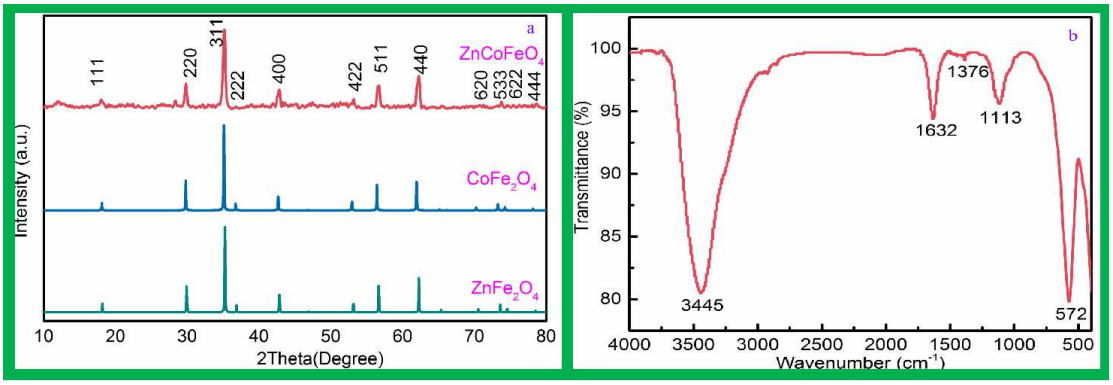

Fig.1 (a) the XRD patterns, (b) FTIR spectrum of copper magnesium ferrite nanoparticles

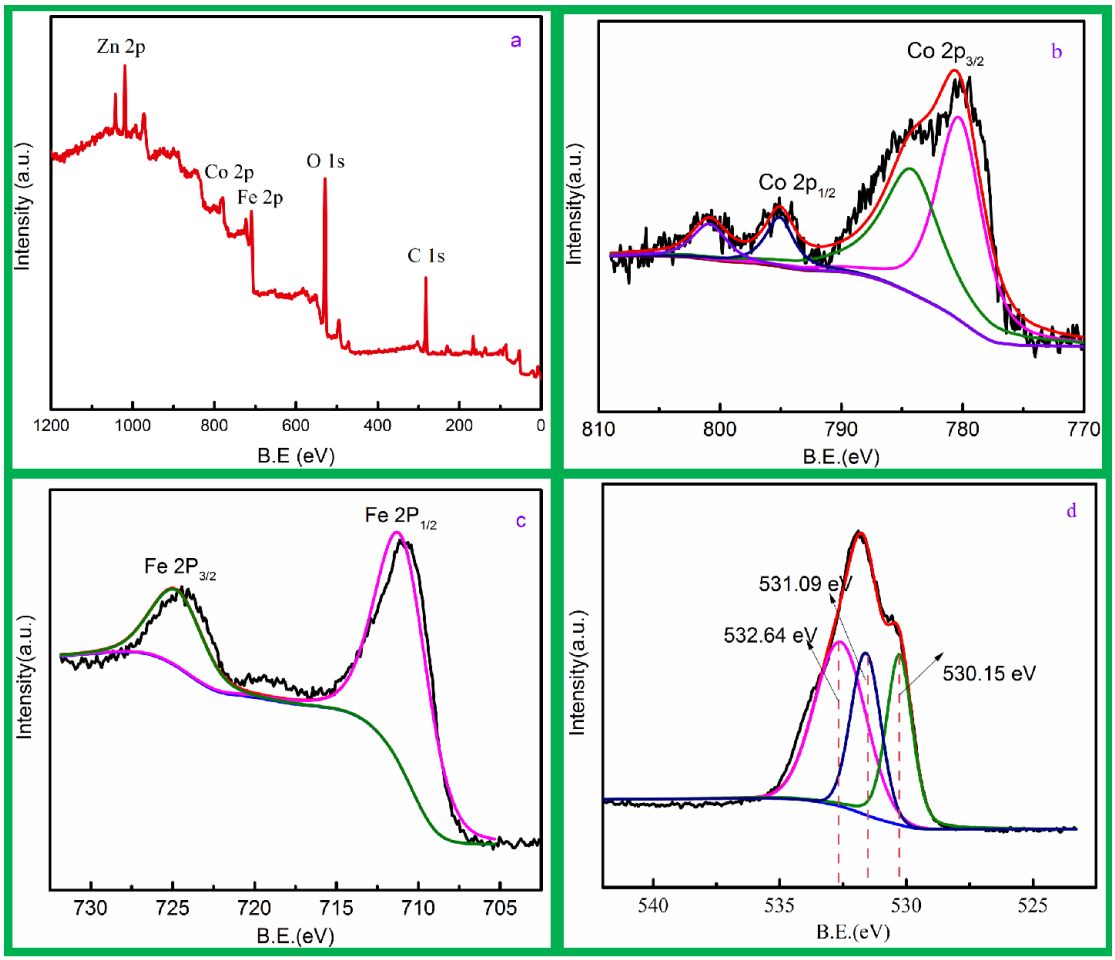

Fig.2 The XPS spectra of (a) wide-scan, (b) Co 2p (c) Fe 2p (d) O 1s of copper magnesium ferrite nanoparticle.

To understand the morphological characteristics of nanomaterials, FE-SEM, and EDS analysis are performed on the prepared materials (as shown in Fig. 3). In Fig. 3a, most of the $CoZnFeO_4$ nanoparticles are uniform with a narrow particle size distribution, and the average particle size is a spherical particle of 30 nm. In addition, there is a certain agglomeration of particles from the figure, which may be due to electrostatic attraction and van der Waals force, some primary particles tend to aggregate in local areas. In Fig. 3b-f, the presence of Fe, Co, O, and Zn by EDS testing indicates that the synthesized substances are made of Fe, Co, O, and Zn. The elemental atlas confirmed that the distribution of Zn, Co, Fe, and O is relatively

uniform, which is beneficial to enhance the catalytic activity.

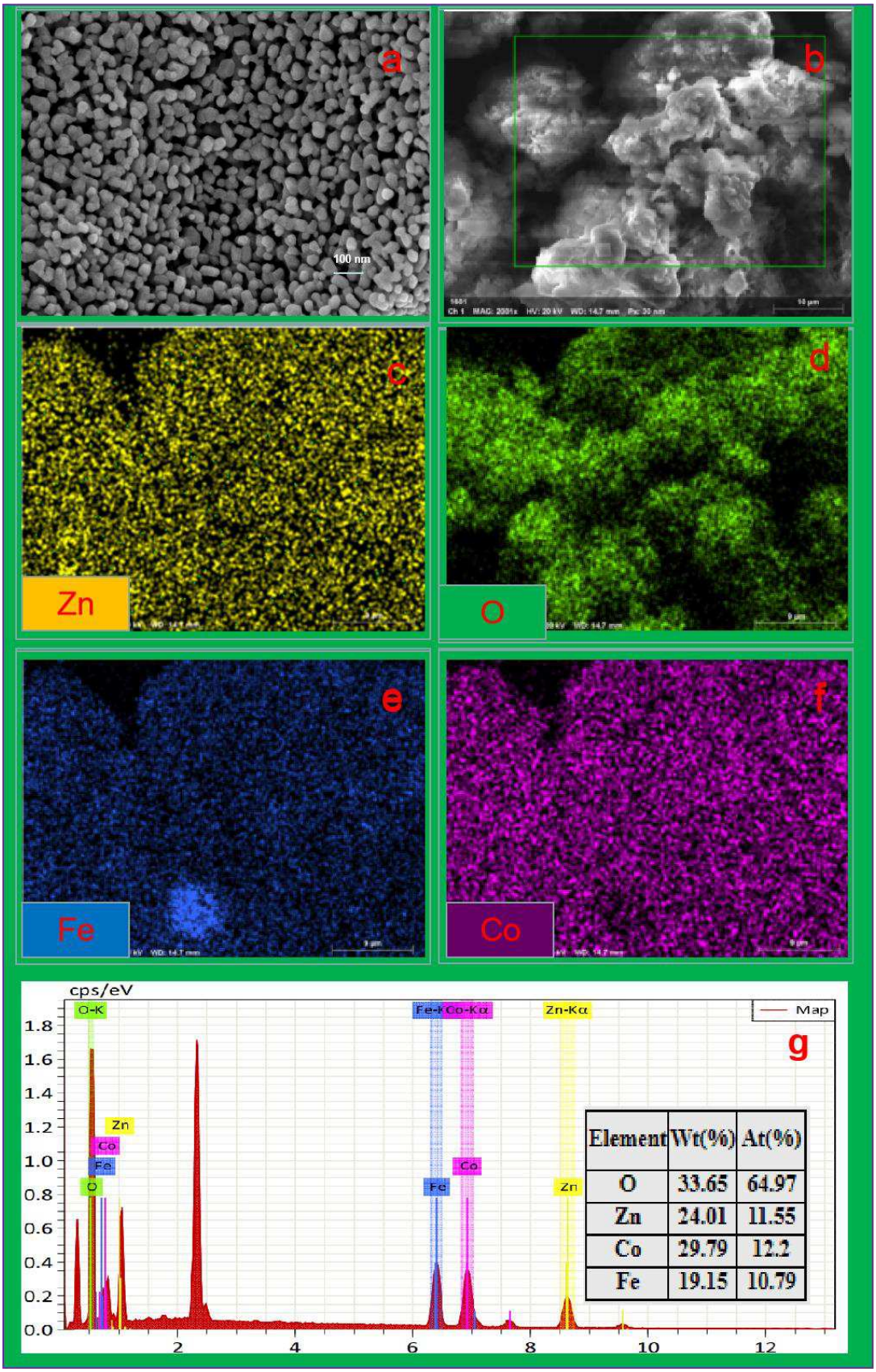

Fig.3 (a) the SEM image, (b-f) EDS patterns of copper magnesium ferrite nanoparticles

198 The adsorption-desorption isotherms of the samples are tested under liquid
199 nitrogen conditions. BET equation is used to calculate specific surface area and the
200 BJH method is used to calculate the aperture from the desorption branch of isotherm.
201 Fig.4a shows the N_2 adsorption-desorption isotherms of the prepared $CoZnFeO_4$ and
202 $ZnFe_2O_4$ nanomaterials. According to the classification of IUPAC, both the
203 $CoZnFeO_4$ spinel oxide and the N_2 adsorption-desorption isotherms of $ZnFe_2O_4$
204 studied are type IV, indicating the mesoporous structure of the prepared materials [19].
205 Also, accompanied by the H1 hysteretic loop, such a strong hysteresis phenomenon is
206 generally believed to be related to capillary condensation of large pore channels [20].
207 As shown in Fig. 4b, the pore diameter of $CoZnFeO_4$ nanomaterials is mainly
208 mesoporous, the pore diameter distribution curve is a single peak, and the pore
209 diameter is mainly centered at 25 nm. The pore diameter distribution of $ZnFe_2O_4$
210 nanomaterials is mainly concentrated around 8 nm. In addition, as shown in Table 3,
211 the total specific surface area and pore volume of $CoZnFeO_4$ are 38.416 m^2/g and
212 0.283 cm^3/g, respectively, and the total specific surface area and pore volume of
213 $ZnFe_2O_4$ are 19.651 m^2/g and 0.066 cm^3/g, respectively. The surface area of the doped
214 zinc ferrite depends on the properties of the dopant. The particle size and specific
215 surface area of the nano-zinc ferrite particles change significantly with the
216 substitution of cobalt. The total specific surface area ratio of $CoZnFeO_4$ is twice that
217 of $ZnFe_2O_4$, which may be caused by the interaction between Co^{3+} and other metal
218 ions (electrostatic effect, ion motion radius). Another reason is that the cobalt atom
219 radius is smaller than the iron atom radius. As the iron atom is replaced, the crystal

size decreases, increasing its surface area [21]. Through comparison, it is found that the surface and pore diameter of $ZnFe_2O_4$ doped with Co^{3+} are significantly larger, which can greatly increase the light-receiving area of the catalyst, reduce the diffusion distance of photogenic carriers, and improve the absorption efficiency of the material to light [22].

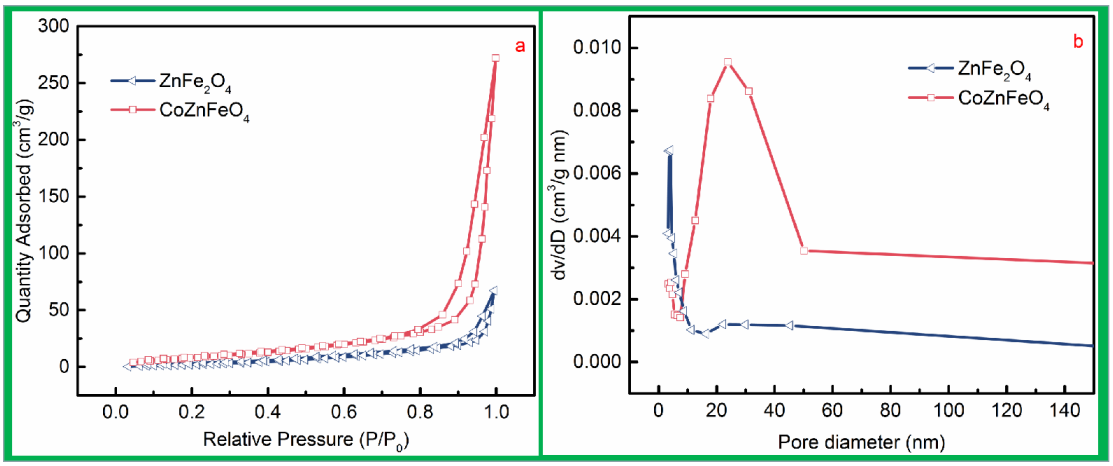

Fig.4 (a) N_2 adsorption/desorption isotherms, and (b) Pore size distribution curves of the $CoZnFeO_4$ and $ZnFe_2O_4$ spinel oxides.

Table 3 Datas of particle size and surface properties of $CoZnFeO_4$ nanocomposites and $ZnFe_2O_4$

Catalyst	Crystallite size D (nm)	Surface area (SBET) (m^2 /g)	Pore size (cm^3/g)
$CoZnFeO_4$	23.66	38.416	0.283
$ZnFe_2O_4$	26.10	19.651	0.066

To compare the redox activity of $CoZnFeO_4$ and $ZnFe_2O_4$, the redox activity is analyzed by the H_2-TPR test. As shown in Fig. 5, there is only one peak of $ZnFe_2O_4$ within the range of 500-700 °C, which is the peak of Fe^{3+} reduced to Fe^{2+}. In contrast,

there are three peaks in $CoZnFeO_4$, which are Co^{3+} reduced to Co^{2+} at 350-450 °C, Fe^{3+} reduced to $Fe^{3+/2+}$ intermediate state at 450-600 °C, and $Fe^{3+/2+}$ converted to Fe^{2+} at 600-800 °C [17]. Multiple reduction peaks appeared in $CoZnFeO_4$, and the initial peak of the reduction peak shifted to a lower temperature. This may be due to the addition of cobalt, so that when Co^{3+}/Co^{2+} is reduced in the same range, Fe^{3+}/Fe^{2+} is also changed, leading to the interference of the reduction curve. As is known to all, reduction reactions first occur on the surface of materials, and the reduction peak moves to the low-temperature zone, which not only proves the surface occupancy of cobalt ions but also indicates that $CoZnFeO_4$ has a strong reduction performance.

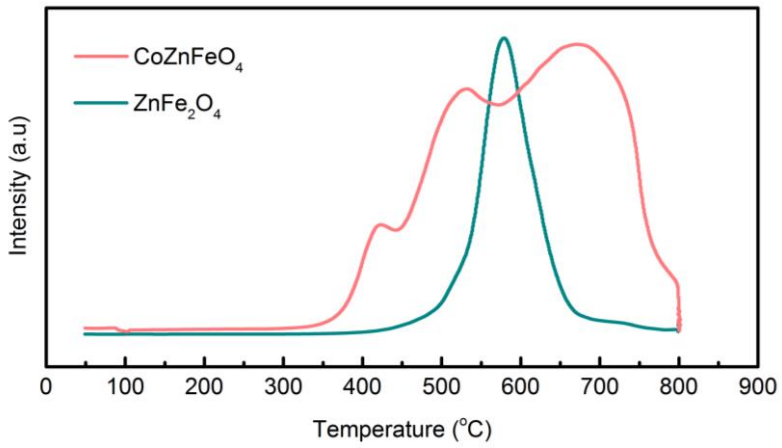

Fig.5 H_2-TPR Profile of $CoZnFeO_4$ and $ZnFe_2O_4$ nanocomposites

3.2 Effects of several parameters on MB decolorization

3.2.1 Study on the decolorizing methylene blue activity of $CoZnFeO_4$ nanomaterials

Fig.6 shows the effect of magnetic $CoZnFeO_4$ nanomaterials synthesized by the solid phase method on the decolorization of MB under different experimental conditions. As shown in Fig. 6, under the condition of H_2O_2 + Light, the

decolorization of MB is only 2.15%, which may be due to the decolorization of MB by hydroxyl radicals generated by the photolysis of H_2O_2 under the Light condition ($H_2O_2 + Light \rightarrow {}^{\cdot}OH + OH^-$) [23]. In the case of $ZnFe_2O_4$ + Dark, the decolorization rate of 30 min MB is only about 2.99%, which may be due to the adsorption effect of $ZnFe_2O_4$ nanomaterials (To exclude adsorption, subsequent experiments are stirred in dark for 1h in advance). However, under the $ZnFe_2O_4$ + Light condition, the decolorization rate is 7.89% within 30 min, higher than that under the no Light condition. This indicates that the catalyst not only has adsorption, but also generates photogenerated electrons and holes (e^-/h^+) excited by $CoZnFeO_4$ under light conditions, and photogenerated holes can directly oxidize MB [24]. Under the condition of $CoZnFeO_4$ + H_2O_2 + Dark, decolorization is completed within 15 min, which may be due to the decomposition of transition metal on H_2O_2 into ·OH, thus promoting the decolorization of MB [25]. Among all the samples, the decolorization rate of $CoZnFeO_4$+H_2O_2+Light is the fastest, which is 46.7% higher than that in the Light condition. This indicates that H_2O_2, as an electron capture agent in the photocatalytic process, can capture photogenerated electrons and separate electron holes, thus improving the efficiency of photocatalysis.

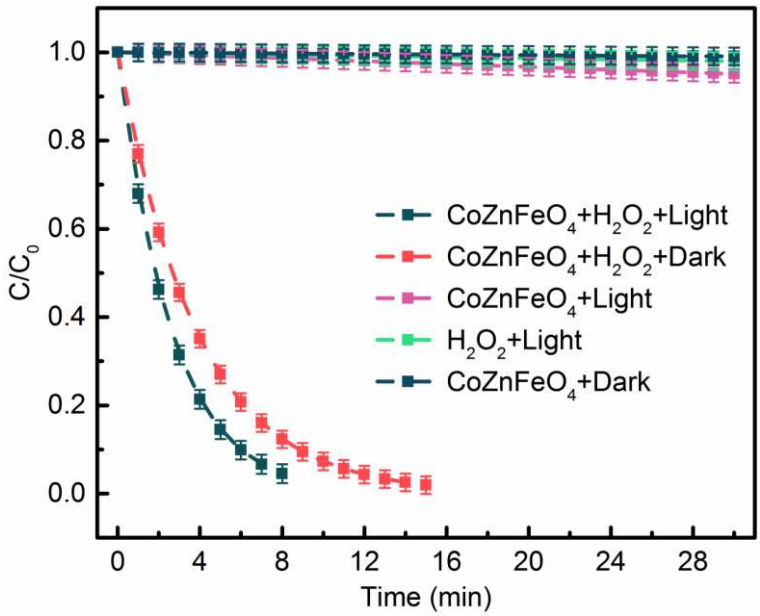

Fig.6. Decolorization rate of MB in different systems. Conditions: solid-to-liquid ratio = 1:500, MB = 200 mg/L, H_2O_2 = 20 mM/L, wavelength = 395 nm, T = 298 K.

3.2.2 Influence of different catalysts on MB decolorization rate

To comprehensively evaluate the decolorization of MB by $CoZnFeO_4$ nanocatalyst, as shown in Fig. 7a, we conducted comparative experiments on the decolorization of MB by using $CoZnFeO_4$, Co_3O_4, Fe_2O_3, Fe_3O_4, and ZnO as catalysts. Within 30 minutes, the decolorization rate of MB is $CoZnFeO_4$ > Co_3O_4 > Fe_2O_3 > Fe_3O_4 > ZnO, and the decolorization rate is 100%, 50%, 40%, 24% and 18%, respectively. $CoZnFeO_4$ decolorized MB at the fastest rate, and the decolorization of MB is completed at the 8th min. This indicates that the coexistence of several metals improves the catalytic activity of catalysts. As shown in Fig. 7b, compared with ZnO, Co_3O_4 and Fe_2O_3 have a faster decolorization rate for MB, which indicates that Fe and Co may have a synergistic effect in the reaction system, which improves the utilization efficiency of photogenerated electrons and the surface-active site of $CoZnFeO_4$ catalyst, thus improving the catalytic efficiency.

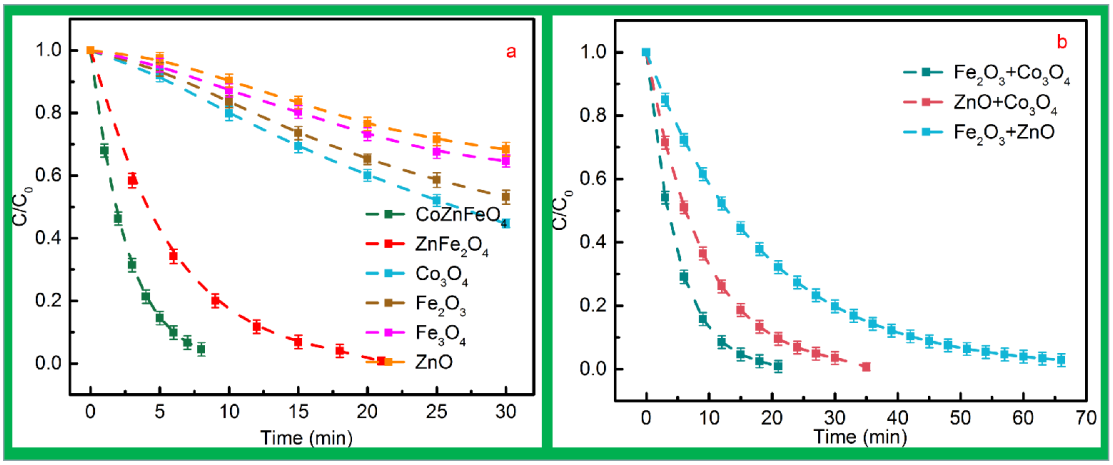

Fig.7. (a)Effect of different catalysts on MB decolorization; (b)Effects of different metal ion combinations on MB decolorization. Conditions: solid-to-liquid ratio = 1:500, MB = 200 mg/L, H_2O_2 = 20 mM/L, wavelength = 395 nm, T = 298 K.

3.2.3 Influence of pH

pH is an important factor in catalytic decolorization because it determines the surface charge properties of the catalyst and the size of the aggregates it forms, which affects the formation and reaction mechanism of free radicals [26]. Fig.8a analyzes the influence of pH value on the photocatalytic decolorization rate. As shown in Fig.8a, the decolorization rate of MB gradually decreases when pH is from 2-10, indicating that pH has a great influence on the degradation of MB.

If catalysis is considered to follow a first-order kinetic equation, the decomposition rate of MB can be calculated using the following equation:

$$\ln(C_0 / C) = kt \quad (2)$$

Where, C_0 is the initial concentration of MB, and C is the concentration of MB at any time. As shown in Fig. 8b, slope constant k of the ratio of $\ln(C_0/C)$ to time under different pH (2, 4, 6, 8, 10) and light illumination conditions. With the increase of pH, the catalytic activity of $CoZnFeO_4$ nanomaterials decreased gradually, leading to a

gradual decrease in rate constant k. As shown in Table 4, the rate constant k at pH=2 is 1.7078 min^{-1}, which is about 10 times faster than the rate constant K at pH=10, which is 0.17147 min^{-1}. This indicates that the catalytic rate of $CoZnFeO_4$ is fast under acidic conditions and that the catalyst can still maintain high catalytic activity in a wide pH range, which is of great value for industrial applications.

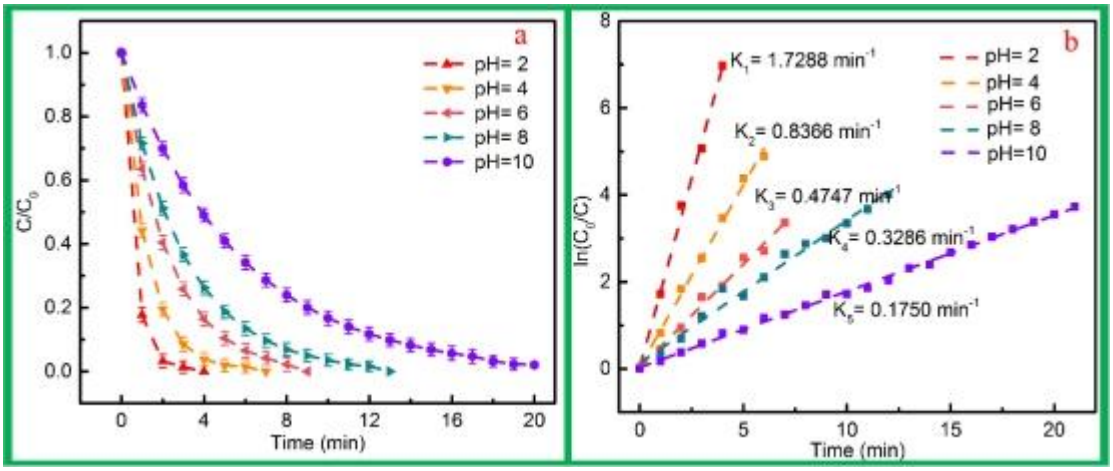

Fig.8. (a) Effect of pH on decolorization rate of MB, (b) Effect of pH on decolorization rate of MB. Conditions: solid-to-liquid ratio = 1:500, MB = 200 mg/L, H_2O_2 = 20 mM/L, wavelength = 395 nm, T = 298 K.

Table 4 Kinetic parameters of MB with different pH drop solutions

pH	k (min^{-1})	R^2
2	1.7288	0.9958
4	0.8366	0.9953
6	0.4747	0.9880
8	0.3286	0.9840
10	0.1750	0.9977

pH value affects the efficiency of the decolorization process and is related to the generation of positive pore, surface coverage, adsorption behavior, and ion leaching rate [70]. To explain the cause of MB decolorization, 0.1g $CoZnFeO_4$ catalyst is dissolved in 50 mL MB solution, and pH is adjusted. Finally, the surface

electromotive force (EMF) of the suspension is measured by ultrasonic under illumination for 20 min. As shown in Fig. 9a, under acidic conditions, the surface of the catalyst is positively charged. According to the infrared analysis of Fig. 1b and XPS analysis of Fig. 2d, it can be seen that the nano-materials synthesized by the solid phase reduction method contain a large number of hydroxyl functional groups, indicating that the variable valence metals mainly exist in Fe-OH and Co-OH. The high concentration of H^+ protonates the surface of nanomaterials, forming functional groups with a positive charge(eq3, eq4). However, when pH is above 8.42, a high concentration of OH^- deprotonates nanomaterials and forms negative charge functional groups on the surface(eq5, eq6) [27,28]. The reaction is as follows:

$$\equiv FeOH + H^+ \rightleftharpoons \equiv FeOH_2^+ \quad (3)$$

$$\equiv CoOH + H^+ \rightleftharpoons \equiv CoOH_2^+ \quad (4)$$

$$\equiv FeOH + OH^- \rightleftharpoons \equiv FeO^- + H_2O \quad (5)$$

$$\equiv CoOH + OH^- \rightleftharpoons \equiv CoO^- + H_2O \quad (6)$$

The relative charge on the surface of nanoparticles is a determining parameter that reflects whether the interaction between particles and the degraded material is repulsive or attractive. According to the DLVO theory, the surface charge properties of nanoparticles are sensitively dependent on their heteroelectron points. When pH is higher or lower than isoelectron (IEP), the surface charge of the particle is positive or negative, respectively. Electrostatic interactions between semiconductor surfaces lead to higher surface coverage, the farther the pH is from IEP, the greater the charge between the particles, the better the particle dispersion [29]. As shown in Fig. 9b,

when pH is 2-8.43, the surface charge of nanoparticles changes from 25.93 mV to -0.36 mV, and IEP is predicted to be 8.3, that is, when pH<IEP, the surface charge of nanoparticles is positive. And positively charged particles will generate positively charged holes (oxidation holes) [30], which can react with hydroxide radicals to generate hydroxyl radicals, thus oxidizing organic compounds. When pH<IEP, the surface positive charge of particles gradually decreases with the increase of pH, that is, the attraction of positive charge holes to hydroxyl radicals decreases, and the rate of producing hydroxyl radicals slows down. Therefore, the decolorization rate of MB decreases as pH increases. Although MB has a positive charge, the negative charge on the surface of the particle at pH>IEP will hinder the generation of oxidized holes, and the decolorization rate depends on the adsorption capacity of MB and the competitive effect of hydroxide on holes. It can be seen from Fig. 8a that the decolorization rate of MB gradually decreases with the increase of pH, indicating that the competition of hydroxide to hole is lower than that of MB, leading to a decrease in the decolorization rate of target substances. When the pH is close to IEP, the particles are severely agglomerated due to the lack of repulsive force, under which case they settle at the fastest rate. In this case, there are fewer particles in the suspension and the oxidation hole is low, so MB has the lowest decoloration rate. However, as shown in Fig. 8a, the decolorization rate is higher than that at pH=10 when pH=8, indicating that the reaction may occur not only on the particle surface but also in the solution. To verify this hypothesis, the concentration of metal ions in the suspension is tested.

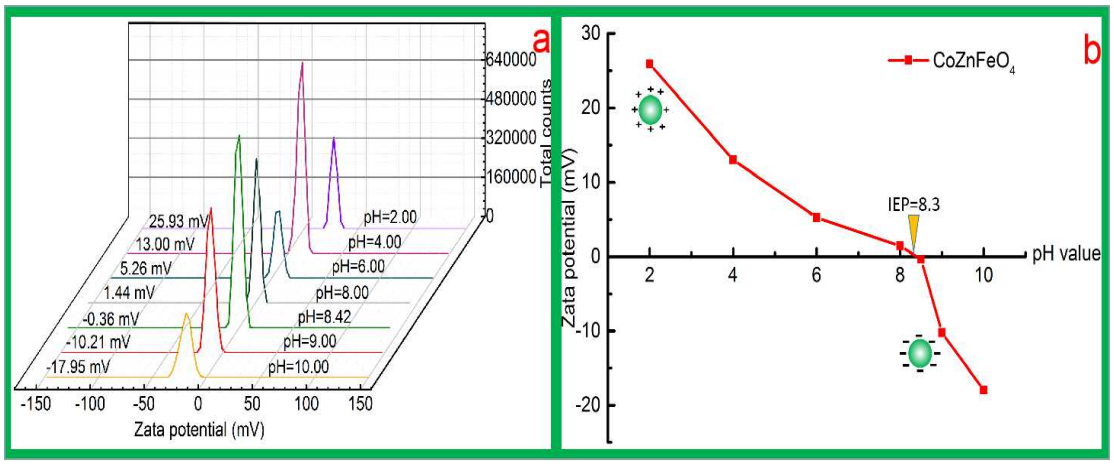

Fig.9. (a) Under different PH conditions, the potential of $CoZnFeO_4$ nanoparticles is easured by Marvin instrument; (b) Zeta potential of $CoZnFeO_4$ nanoparticles as a function of pH.

The content of metal ions in the solution is tested by ICP-MS, as shown in Table 5. Under different pH values (2, 4, 6, 8, 10), with the rise of pH, the leaching rate of metal ions gradually decreased, and the decolorization rate of MB gradually decreased, indicating that metal ions in the solution may have a certain role in the decolorization process of MB [31]. In photocatalysis, transition metal ions in solution capture electrons, which are easily transferred to H_2O_2 to form hydroxyl radicals(eq7, eq8). The hydroxyl radicals produced are very reactive substances that react with most organic matter. At the same time, H_2O_2 as an electron capture agent can also capture photogenerated electrons (e^-) (eq9), thus enabling the separation of photogenerated electrons from photogenerated holes and improving the efficiency of photocatalysis [32]. The specific reaction is as follows:

$$M^{3+} + e^- \rightarrow OH^- + {}^{\bullet}OH \quad (7)$$

$$M^{2+} + H_2O_2 \rightarrow M^{3+} + OH^- + {}^{\bullet}OH \quad (8)$$

$$H_2O_2 + e^- \rightarrow OH^- + {}^{\bullet}OH \quad (9)$$

However, although pH=2 has the fastest decolorization rate of MB, it will cause excessive dissolution of metal elements, which may lead to excessive heavy metals in the water. Therefore, in the subsequent experiments, we will try to choose a more appropriate pH for the experiment.

Tabel 5 The leaching amount of Fe^{3+}, Zn^{2+} and Co^{3+} at different pH

pH	2	4	6	8	10
Fe^{3+} leaching(μg/L)	22.27	16.46	14.46	13.09	11.34
Zn^{2+} leaching(μg /L)	56.77	48.47	45.71	45.68	45.64
Co^{3+} leaching(μg /L)	55.43	41.08	37.24	32.62	27.36

3.2.4 Influence of light wavelength on methylene blue decolorization

Through UV-Visible diffuse reflection absorption spectrum, the optical absorption properties of synthetic materials within the range of UV-Visible spectrum can be explored, and the bandwidth of the material can be calculated, and then the photocatalytic ability of the material can be inferred indirectly. Fig. S10 shows the bandgap width of the catalyst is 2.02 eV, which is consistent with literature reports [35], and the lower the energy required for the electron transition reaction, the easier the photocatalysts, and Lan [36] reported bandgap of $ZnFe_2O_4$ is 2.11eV. This indicates that the doping of Co, which replaces the position of Fe, forms impurity levels in the bandgap and reduces the energy required for electron transition, which is beneficial to the light absorption capacity.

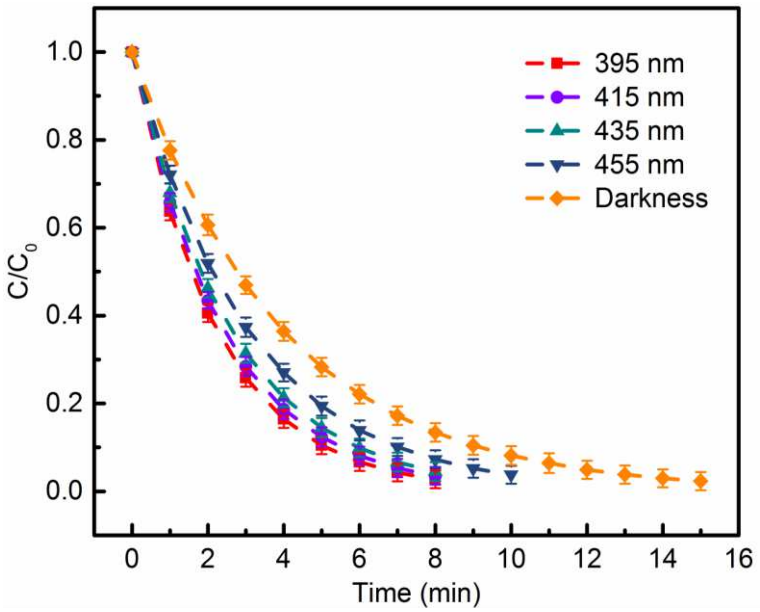

Fig.11. Effect of the wavelength on the decolorization of MB. Conditions: solid-to-liquid ratio = 1:500, MB = 200 mg/L, H_2O_2 = 20 mM/L, wavelength = 395 nm, T = 298 K.

In this work, the optimal wavelength of MB decolorization is studied. As shown in Fig. 11, the decolorization efficiency gradually decreases with the increase of wavelength, which is consistent with the UV-Vis test results. The light wavelength reflects the energy intensity of incident light and is directly related to electron transition, which determines the concentration of hydroxyl radical produced. However, due to the presence of an appropriate concentration of H_2O_2, it also has a better decolorization effect under dark conditions.

3.2.5 Influence of hydrogen peroxide concentration on MB decolorization rate

The H_2O_2 concentration is an important factor affecting MB decolorization in photocatalytic reactions. As shown in Fig. 12, the decolorization rate of MB increases, and decolorization time shorten with the increase of H_2O_2 concentration. When the concentration of H_2O_2 increases from 20 mM to 25 mM, the overdosing of H_2O_2 will decrease the decolorization rate of MB. At a low H_2O_2 concentration, the

improvement of the decolorization rate may be due to the following reasons. Firstly, The H_2O_2 can produce hydroxyl radical under light conditions due to the main rate improvement mechanism for this process (eq10). Ollis [37] and Ilisz [38] suggest the possible mechanisms in the H_2O_2 is considered to be a better electron acceptor than oxygen which will reduce the chances of electron-hole pair recombination, which may result in a hydroxyl radical (eq11) rather than a weak radical (eq12) [39]. This shows that the more HO• can be used for MB oxidation at the appropriate range of the H_2O_2 adding. However, at the high H_2O_2 doses, the excess H_2O_2 molecules clear HO• (eq13) generated by direct photolysis of H_2O_2 [40,41], or the oxidation of h^+ with OH^- (eq14) to a less oxidizing (eq15) [42]. Therefore, accession H_2O_2 becomes an inhibitor of MB removal. In the rest of the study, the use concentration of H_2O_2 is determined as 20 mM.

$$H_2O_2 + HO^{\bullet} \rightarrow H_2O + HO_2^{\bullet} \quad (10)$$

$$H_2O_2 + e^- \rightarrow HO^{\bullet} + OH^- \quad (11)$$

$$O_2 + e^- \rightarrow {}^{\bullet}O_2^- \quad (12)$$

$${}^{\bullet}OH + H_2O_2 \rightarrow H_2O + HOO^{\bullet} \quad (13)$$

$$h^+ + OH^- \rightarrow HO^{\bullet} \quad (14)$$

$$H_2O_2 + HO^{\bullet} \rightarrow H_2O + HO_2^{\bullet} \quad (15)$$

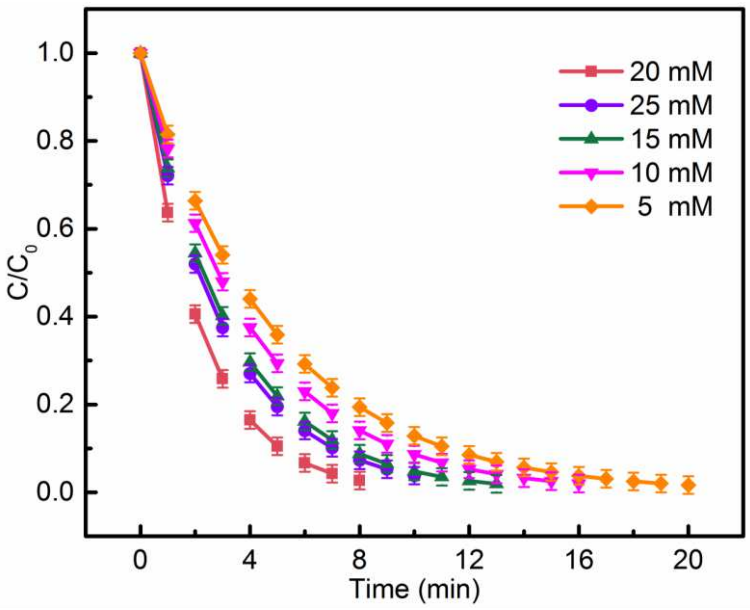

Fig.12. Effect of hydrogen peroxide concentration on the decolorization rate of MB. Conditions: solid-to-liquid ratio = 1:500, MB = 200 mg/L, H_2O_2 = 20 mM/L, wavelength = 395 nm, T = 298K.

3.2.6 Influence of $CoZnFeO_4$ dosage on MB decolorization rate

From the economic point of view, the amount of catalyst is one of the important parameters in decolorization MB. To choose the adding of catalysts, it is necessary to determine the optimal amount of load for the effective removal of MB dyes. The effect of the catalyst load on dye removal rate is investigated, and the results are shown in Fig. 13. As can be seen, the decolorization rate of MB gradually increases with the increase of catalyst dosage from 0.5-1.0 g/L. This is due to an increase in the number of active sites, and the more active sites there are, the more opportunities there are to receive light. However, when the amount of catalyst increased from 1.0 g/L to 3.0 g/L, the decolorization rate decreased, which may be because the high concentration of catalyst led to the aggregation of catalyst particles, which led to the reduction of the number of surface active sites and reduced the catalytic efficiency.

458 Besides, the high concentration of catalyst will increase the opacity of suspension and
459 the scattering of light, thus reducing the number of times that the irradiated light
460 passes through the catalyst. In this study, economic and environmental factors are
461 taken into account to determine the optimal catalyst usage of 1.0 g/L.
462

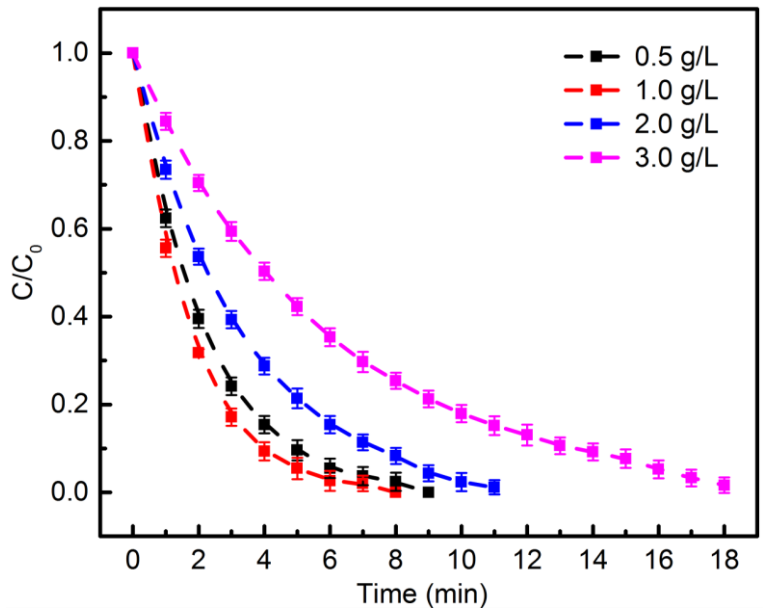

463
464 **Fig.13**. Effect of catalyst dosage on the decolorization of MB.Conditions: wavelength = 395 nm,
465 H_2O_2 = 20 mM/L, T = 298 K.
466
467 **3.2.7 Influence of methylene blue concentration on decolorization rate**
468 The effect of MB concentration from 200 mg/L to 500 mg/L on decolorization
469 rate is investigated under the optimal conditions of the dosage $CoZnFeO_4$ under the
470 given wavelength. As shown in Fig. 14, the time for decoloration of MB is extended
471 from 6 min to 12 min with the initial concentration of MB increasing from 200 mg/L
472 to 500 mg/L. Photocatalytic decolorization is completely dependent on the generation
473 of hydroxyl radicals and positively charged holes. However, with the increase of MB
474 concentration, the hydroxyl radical yield is decreased, resulting in the decolorization

rate decreased. Moreover, with the continuous increase of MB concentration, MB molecules per unit volume increase and occupy more active sites [43,44]. Besides, lots of dye molecules hinder the utilization efficiency of light [45]. Therefore, in photocatalytic decolorization, the decolorization rate decreases with the increase of MB concentration.

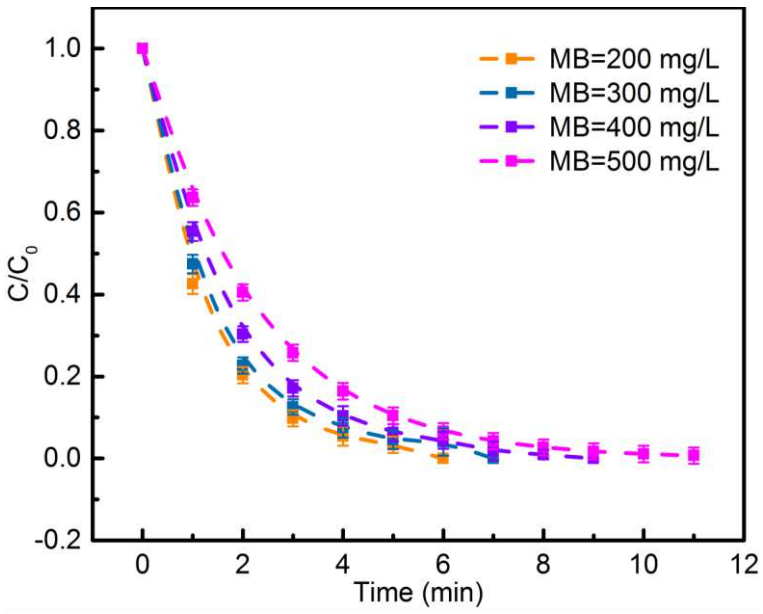

Fig.14. Effect of MB concentration on decolorization rate. Conditions: wavelength = 395 nm, solid-to-liquid ratio = 1:1000, T = 298 K.

3.2.8 Effect of temperature on decolorization MB

Temperature is one of the important factors of photocatalysis. The effect of temperature (15 °C, 25 °C, 35 °C, 45 °C) on the decolorizing MB reaction rate constant of $CoZnFeO_4$ is studied. As can be seen from Fig. 15a, the reaction rate constant gradually increases with the rise of temperature, indicating that the leaching of $CoZnFeO_4$ metal ions may be an endothermic process [46].

The higher temperature is favorable for $CoZnFeO_4$ decolorization MB reaction because the higher temperature can provide energy for reactant molecules to

overcome the activation energy barrier [47]. Therefore, the kinetic constants of the generation of free radicals and the regeneration of Fe^{3+}/Fe^{2+} and Co^{3+}/Co^{2+} increase with the rise of temperature [48,49]. Miller and Sotolongo established the relationship between the reaction temperature and the decomposition rate constant of H_2O_2. The results show that at a certain temperature, the decomposition rate of H_2O_2 is accelerated with the increase of temperature, thus promoting the generation of HO• [50].

Through experiments at different temperatures, the Arrhenius equation (eq16) is used to calculate the activation energy of the reaction [51]:

$$K = A \exp\left(-\frac{E}{RT}\right) \quad (16)$$

Where A is the front factor, E is the apparent activation energy ($J \cdot mol^{-1}$), R is the ideal gas constant (8.314 $J \cdot mol^{-1}K^{-1}$), and T is the reaction temperature (K).

The Arrhenius diagram of lnk and 1/T is shown in Fig. 16b, there is a good linear relationship between the natural lnK and 1/T. Activation energy E obtained from Arrhenius in Fig. 15b is 31.102 $KJ \cdot mol^{-1}$, and A value is 1.157×105 $M^{-1}min^{-1}$. In general, reaction activation energies for general thermal reactions are between 60 $KJ \cdot mol^{-1}$ and 250 $KJ \cdot mol^{-1}$ [52].

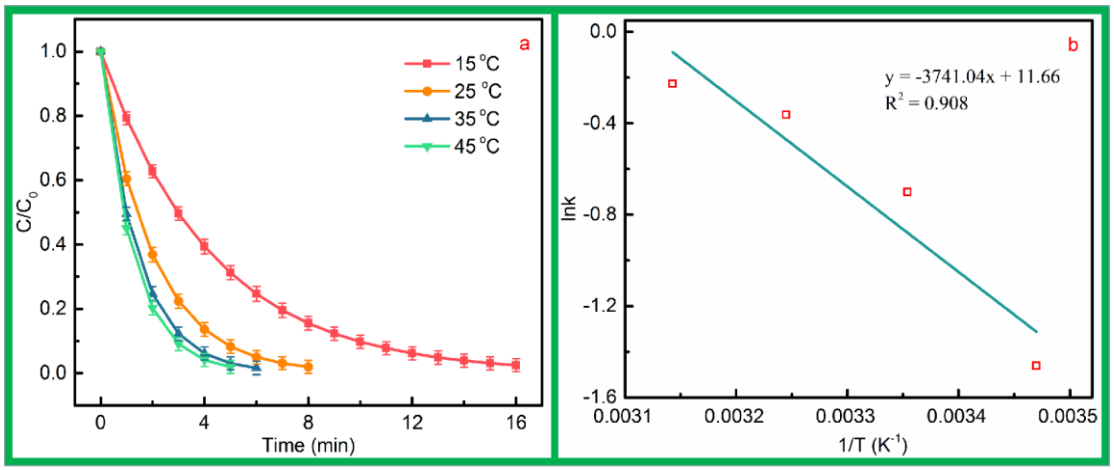

Fig.15. (a) Effect of temperature on the catalytic performance of $CoZnFeO_4$, (b) the Arrhenius plot of lnk versus 1/T of the decolorization of MB by photocatalytic. Conditions: solid-to-liquid ratio = 1:1000, MB = 200 mg/L, H_2O_2 =20 mM/L, wavelength: 395 nm.

3.2.9 Comparison of decolorization MB with other catalysts

As shown in Table 6, the decolorization performance of the synthesized $CoZnFeO_4$ catalyst for MB is compared with other catalysts reported in the literature [52-57]. It can be observed that $CoZnFeO_4$ decolorizes MB within 8 min under normal pH. This indicates that the nanocatalysts prepared from waste materials have better catalytic activity than other catalysts. It also proves that the method of site control has the prospect of large-scale industrialization.

Table 6 Comparison of performance of $CoZnFeO_4$ catalyst with some previously reported catalyst for MB decolorization.

Catalyst	Decolorization process	Initial pH	MB (mg/L)	Catalyst amount	Oxidant/ Reductant	Decolorization time	Removal Efficiency(%)	Reference

$CoZnFeO_4$	Photo-catalytic	5.78	200	1 g/L	H_2O_2 20 mM/L	8 min	100.0	this study
α-Bi_2O_3 NPS	Photo-catalytic	2.00	10	1 g/L	100mL 1:5 HNO_3:H_2O	90 min	90.0	[17]
$CoMnFeO_4$	Photo-catalytic	2.00	15	20 mg/L	1:50 H_2O_2:MB	20 min	99.3	[18]
$ZnO/CaFe_2O_4$	UV	2.00	32	2 g/L	30% 2mL H_2O_2	20 min	57.0	[19]
$Ag_3VO_4/CaFe_2O_4$	Photo-catalytic	No data	32	2 g/L	No data	60 min	59.3	[20]
$ZnFe_2O_4$	λ>420 nm	13.00	10	1 g/L	None	360 min	8.0	[21]
Fe_3O_4	None	No data	100	30 g/L	H_2O_2 2.5 M/L	50 min	10.0	[22]

525

526 **3.3 Structure and stability of the catalyst**

527 The application of catalyst in wastewater treatment requires it to be stable for
528 metal ion leaching in the liquid phase under operating conditions. Continuous and
529 progressive leaching not only leads to deactivation of the catalyst but also pollute
530 water further.

531 Stability is one of the key factors affecting the catalyst application [58]. In this
532 study, $CoZnFeO_4$ samples are continuously used 5 times under the same conditions to

evaluate the maintenance of their photocatalytic activity. Among them, MB is photocatalysts decolorization, $CoZnFeO_4$ particles are recovered (such as centrifugation and magnetic adsorption), organic pollutants are removed with deionized water and ethanol, and finally, freeze-drying is carried out. As can be seen from Fig 16a, within 5 cycles, the decolorization rate of MB does not change significantly, and the complete decolorization of MB is completed within 12 min. This indicates that the $CoZnFeO_4$ catalyst can maintain high catalytic activity after repeated use many times. However, after 5 cycles, the decolorization rate is slightly slowed down, which may be because of the continuous operation. In addition to, the slight inactivation caused by metal leaching, it may also be due to the deposition of carbon compounds in the active part of the catalyst, resulting in the decrease of activity [59]. As shown in Fig. 16b, by comparing the XRD patterns of $CoZnFeO_4$ before and after the reaction, there is no obvious change. At the same time, it can be seen from Fig. 18a that the FTIR of $CoZnFeO_4$ catalyst did not change significantly before and after the reaction, which also indicated that the $CoZnFeO_4$ nanometer material maintained a good reuse performance and a long service life. Besides, as shown in Fig. 17b, compared with other reported results [58], the leaching amount of metal ions in the reaction mixture (g/L) is quite low. Among them, the leaching amount of Co^{3+} ions is higher than that of Fe^{3+}, indicating that the interaction between Co^{3+} ions and reactants is greater than that of Fe^{3+}, that is, the surface occupancy rate of Co^{3+} is higher. As shown in Fig. 18, the EDS of $CoZnFeO_4$ after reaction shows that the metal elements still maintain a relatively uniform distribution, which indicates

the stability of the octahedral structure in spinel ferrite. Meanwhile, by comparing the mass fraction of metal ions in Fig. 18f, the leaching rate of Co^{3+} and Zn^{2+} after the reaction is higher than that of Fe^{3+}, which is consistent with the test structure in Fig.18b, that is, the surface occupancy rate of Co^{3+} is higher.

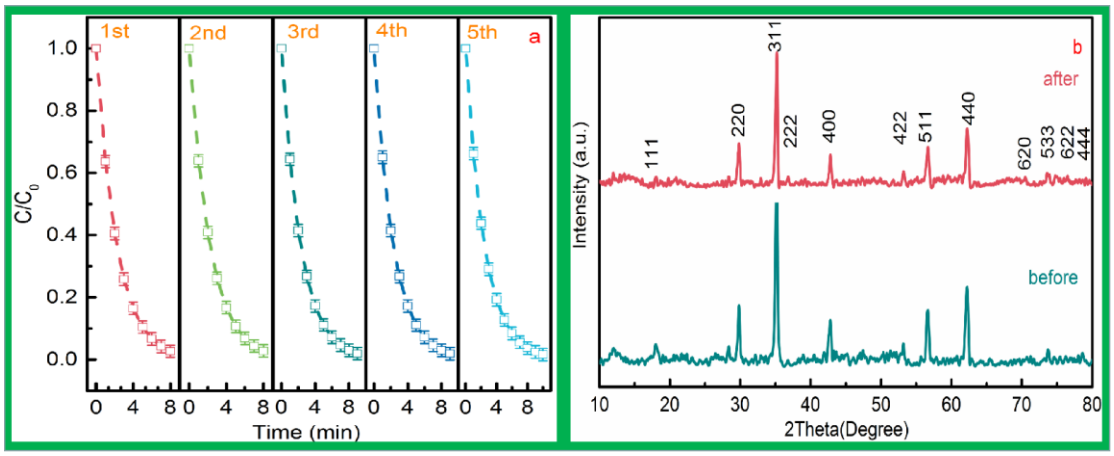

Fig.16. The reusability of $CoZnFeO_4$ for MB decolorization in the presence of light (a); XRD patterns of $CoZnFeO_4$ before and after the reaction (b). Conditions: solid-to-liquid ratio = 1:1000, MB = 200 mg/L, H_2O_2 = 20 mM/L, wave=length = 395 nm, T = 300.15 K.

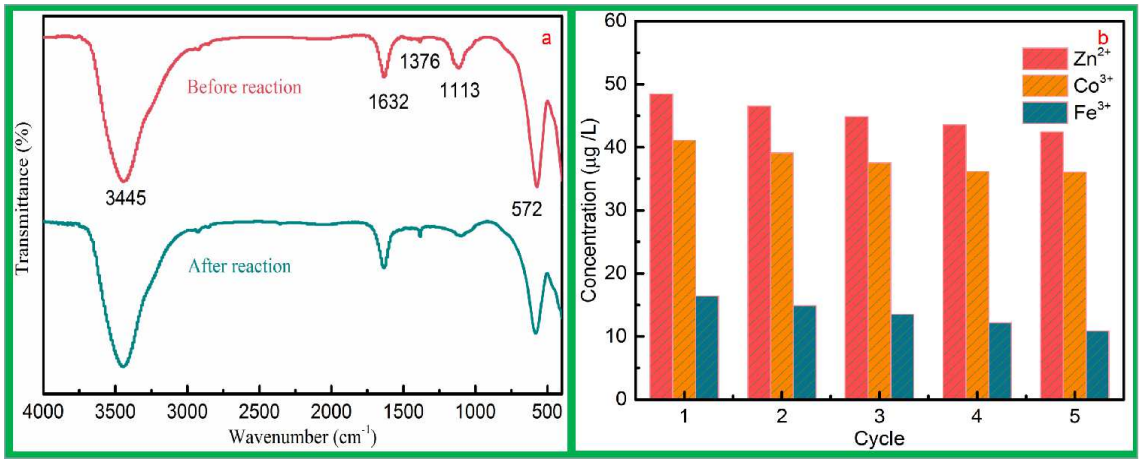

Fig.17. FTIR patterns of $CoZnFeO_4$ before and after the reaction (a); The leaching amount of Zn^{2+}, Co^{3+} and Fe^{3+} after cyclic decolorization of $CoZnFeO_4$ for 5 times (b). Conditions: solid-to-liquid ratio = 1:1000, MB = 200 mg/L, H_2O_2 = 20 mM/L, wavelength = 395 nm, T = 300.15 K.

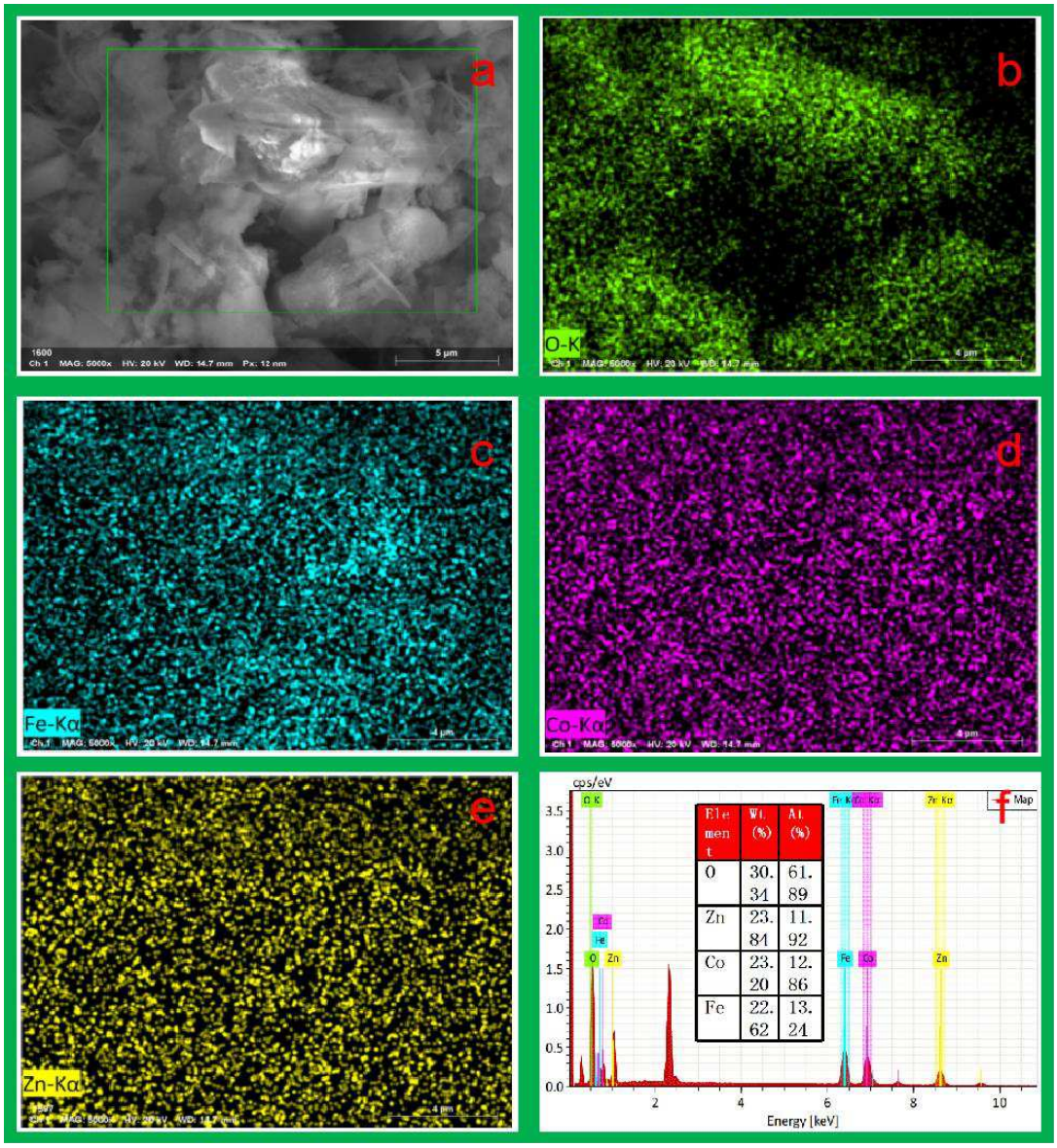

Fig.18. EDS element mapping area (a); EDS elemental mapping of O (b), Fe (c), Co (d), Zn (e); Energydiapersive X-ray spectroscopy (EDS) patterns of CoZnFeO4 (f).

3.4 Decolorization mechanism

To study the active components in the photocatalytic bleaching MB reaction of $CoZnFeO_4$, tert-butanol (TBA), ethylene diamine tetraacetic acid (EDTA), 1, 4-benzoquinone (BQ), and copper nitrate (CN) are selected as the capture agents to scavenging hydroxyl radical (HO•), hole (h^+), superoxide radical ($O_2^{\bullet-}$) and electron

579 (e^-) [44]. Fig. 19 shows the effects of different scavengers on the photocatalytic
580 activity of $CoZnFeO_4$.

581 It is found that in the presence of BQ, the decolorization effect of MB is not
582 significant, indicating that $O_2^{\bullet-}$ is not the main factor determining the photocatalytic
583 decolorization of MB by $CoZnFeO_4$. After the addition of TBA, CN and EDTA, the
584 decolorization rate of MB decreased from 100% to 49%, 67% and 81% within 5 min.
585 These results indicated that HO• and hole (h^+) are the main active substances in the
586 process of $CoZnFeO_4$ decolorization of MB. In the presence of electron-trapping CN,
587 reactive oxygen species($O_2^{\bullet-}$, HO•) cannot be generated because conductive electrons
588 (e^-) cannot be reduced to oxygen [60]. Therefore, the decolorization of dyes is not
589 significantly inhibited under visible light irradiation, that is, e^- play a secondary role
590 in this process [61,62]. At the same time, it can be seen in the figure that compared to
591 the ideal state, the presence of N_2 has been decolorized by about 97% MB. This
592 verifies that the whole reaction is not formed, that N_2 is not inhibited in the reaction
593 [63]. Therefore, we conclude that the presence of O_2 in the reaction has less effect on
594 the process.

595 To further analyze the reaction mechanism of the system, it is realized by
596 photoluminescence characterization. The intensity of PL emission reflects the
597 recombination rate of photogenic electron-hole pairs [64]. In general, lower intensity
598 indicates rapid transfer or annihilation of excited electrons, while higher intensity
599 indicates a high rate of recombination of excited electrons [65]. Fig. 20 shows the
600 $CoZnFeO_4$ and $ZnFeO_4$ systems excited by 350 nm. It can be seen that the emission

intensity of $CoZnFeO_4$ samples is significantly lower than that of $ZnFeO_4$, which indicates that the charge transfer and separation capability of $CoZnFeO_4$ are relatively strong. Among them, the peaks at 415.09 nm and 435.26 nm correspond to characteristic near-band-Edge (NBE) blue emission, which is mainly attributed to the characteristic NBE blue emission, namely intermittent zinc deficiency, which is caused by the recombination of electrons in oxygen vacancies and photogenic holes generated at tetrahedral and octahedral positions [65-67]. The peaks at 627.13 nm and 569.40 nm are due to the transition of Fe^{3+} from $3d^5$ to $3d^4$ 4s. The conduction band electrons from the 3d5 state balance the 4S orbital of Fe 3p [68]. Compared with $CoZnFeO_4$, the lower PL emission intensity is because doping Co ions can produce a large number of defects, reduce the luminescence intensity of zinc ferrite, and lead to the reduction of photoelectron-hole pair recombination rate. In the process of MB photocatalysis, when the visible light energy larger than the energy gap irradiates the catalyst, the electrons move to the conduction band, and the valence band thus produces photogenic holes. Valence band electrons (e^-) are excited to the conduction band of the $CoZnFeO_4$ catalyst. Then the valence band generates photogenic holes (h^+), oxidizes H_2O into HO•, and forms (-OH) hydroxyl group on the surface of the $CoZnFeO_4$ nanometer sheet after adsorption. The photogenerated electron has high electron mobility, which can decompose O_2 into •OH. The separation of holes and photogenerated electrons leads to a decrease in the recombination rate between them and leads to the migration of more charge carriers to the surface of the $CoZnFeO_4$ nanosheet [38-40]. The unpaired photogenerated electrons in the conduction band can

generate hydroxyl radicals with H_2O_2, while the holes in the valence band can also react with H_2O to generate hydroxyl radicals, and then decolorize MB dyes [69].

To determine the chemical state changes and reaction mechanism of $CoZnFeO_4$ before and after decolorizing MB, XPS is used to analyze the samples. As shown in Fig. 21a, the peak position before and after the reaction did not deviate significantly, indicating that the $CoZnFeO_4$ octahedral structure is stable and no lattice distortion occurred. At the same time, there is an extra N spectrum after the reaction, which may be caused by the residue of small molecules broken in MB on $CoZnFeO_4$. Fig. 21b-c shows the high-resolution XPS spectrum of Fe $2p_{3/2}$ between 705 ~ 720 eV before and after the catalytic reaction [70]. Peaks of Fe(III) and Fe(II) ions correspond to 712.6 eV and 710.5 eV, respectively [71,72]. After the reaction, the proportion of Fe(II) increased to 32.93% and the proportion of Fe(III) decreased to 62.07%, indicating that part of Fe(III) is converted into Fe(II) ions. Fig 19d-e also shows the XPS spectra of Co $2p_{3/2}$ at 770 ~ 810 eV [73]. After the reaction, the proportion of Co(II) increased to 43.63% and decreased to 56.37% compared with Co(III), indicating that part of Co(III) changed to Co(II) [74,75]. In Fig. S22, the values of the conduction band and valence band are calculated theoretically. In Fig. 23, the maximum binding energy of Zn $2p_{3/2}$ in f-g is about 1022.5 eV [76,77], indicating that the valence of Zn^{2+} did not change before and after the reaction. These results showed that both Fe^{3+}/Fe^{2+} and Co^{3+}/Co^{2+} are involved in catalytic reactions, and the amount of cobalt valence transformation is greater than that of iron, indicating that Co^{3+}/Co^{2+} have a prominent influence in the whole reaction.

According to the free radical capture experiment and XPS spectral analysis, the decolorization of MB is mainly carried out through the decomposition of H_2O_2 into hydroxyl radicals and the h^+ generated by the catalyst.

Pathway 1: As shown in Fig. 23, the oxidation potential of Co(III)/Co(II) (1.81V) is higher than that of Fe(III)/Fe(II) (0.77 V) [78], so Co^{3+} reacts first with H_2O_2 to produce Co^{2+}. Fe^{3+} reacts with H_2O_2 to form Fe^{2+} and •OOH and H^+. •OOH is less oxidizing than H_2O_2, so H_2O_2 preferentially continues to oxidize with Co^{2+}. Meanwhile, according to the front-line molecular orbital theory, electrons will flow from the less electronegative elements to the more electronegative elements, so electrons Fe^{2+} (4.06eV) will flow to Co^{3+} (4.3eV), realizing the recycling of Fe^{3+}/ Fe^{2+} [79,80]. And then Co^{2+} reacts with H_2O_2 to form Co^{3+} and HO•, to complete the recycling of Co^{3+} over Co^{2+}, complete the recycling of Co^{3+}/ Co^{2+}. Next, HO• will react with MB to generate carbon dioxide and water to complete the degradation process [81]. The specific reaction steps are shown below:

$$Co^{3+} + H_2O_2 \rightarrow Co^{2+} + {}^{\cdot}OOH + H^+ \quad (17)$$

$$Fe^{3+} + H_2O_2 \rightarrow Fe^{2+} + {}^{\cdot}OOH + H^+ \quad (18)$$

$$Co^{2+} + H_2O_2 \rightarrow Co^{3+} + HO^{\cdot} + OH^- \quad (19)$$

$$Fe^{2+} + Co^{3+} \rightarrow Fe^{3+} + Co^{2+} (E_0=1.04\ V) \quad (20)$$

$$Co^{2+} + H_2O_2 \rightarrow Co^{3+} + HO^{\cdot} + OH^- \quad (21)$$

$$MB + HO^{\cdot} \rightarrow CO_2 + H_2O \quad (22)$$

Pathway 2: When visible light irradiates the semiconductor, the band gap (<3.147 eV) is larger than that of the catalyst (2.02 eV). Some of the electrons in the

valence band will be excited and jump from the valence band over the forbidden band to the conduction band, thus generating photogenic electrons and h^+ respectively in the conduction band and the valence band [82]. The conduction band gap (0.3975 eV) of $CoZnFeO_4$ is not lower than that of $CoZnFeO_4$ (-0.33 eV); therefore, electrons in the conduction band cannot react with oxygen molecules to form superoxide radicals [58]. On the contrary, the photogenerated electrons in the $CoZnFeO_4$ conduction band react with H_2O_2 to produce more, which leads to the oxidation reaction. Moreover, the hole (h^+) has a high oxidation potential, which can lead to direct oxidation of MB. At the same time, the valence band of $CoZnFeO_4$ (2.41 eV) has a higher potential than that of (1.99 eV), so that the hole can directly participate in the oxidation of MB, and can also react with hydroxide ions to generate hydroxyl radical. So under the action of hydroxyl radicals and holes, it leads to the decolorization of MB. The decolorization mechanism is shown as follows:

$$CoZnFeO_4 + hv \rightarrow e^-_{(CB)} + h^+_{(VB)} \quad (23)$$

$$e^- + H_2O_2 \rightarrow HO^{\bullet} + OH^- \quad (24)$$

$$MB + (^{\bullet}OH, h^+_{vb}) \rightarrow CO_2 + H_2O \quad (25)$$

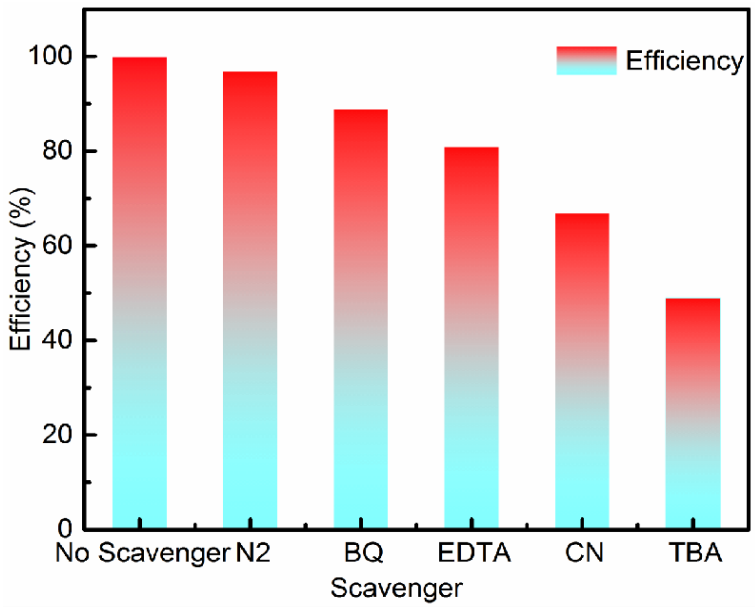

683

684 **Fig.19**. PhotoDecolorization of MB by Nano-$CoZnFeO_4$ in the presence of different scavengers.

685

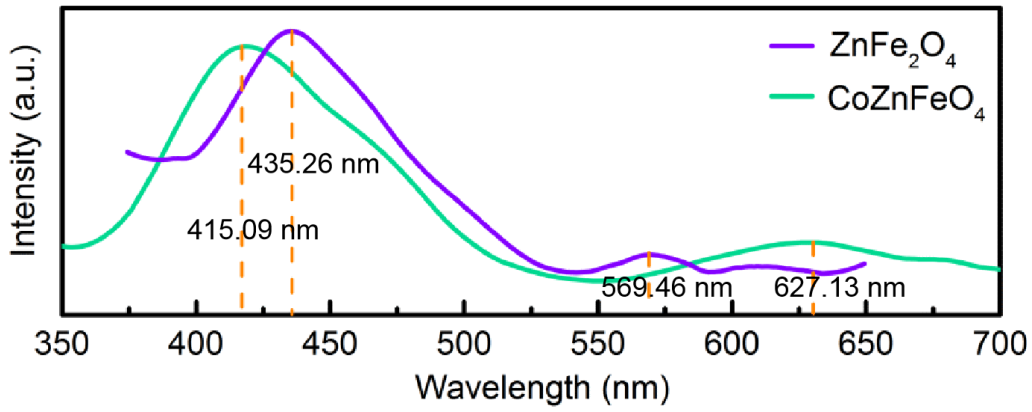

686

687 **Fig.20**. The PL spectra of the $CoZnFeO_4$.

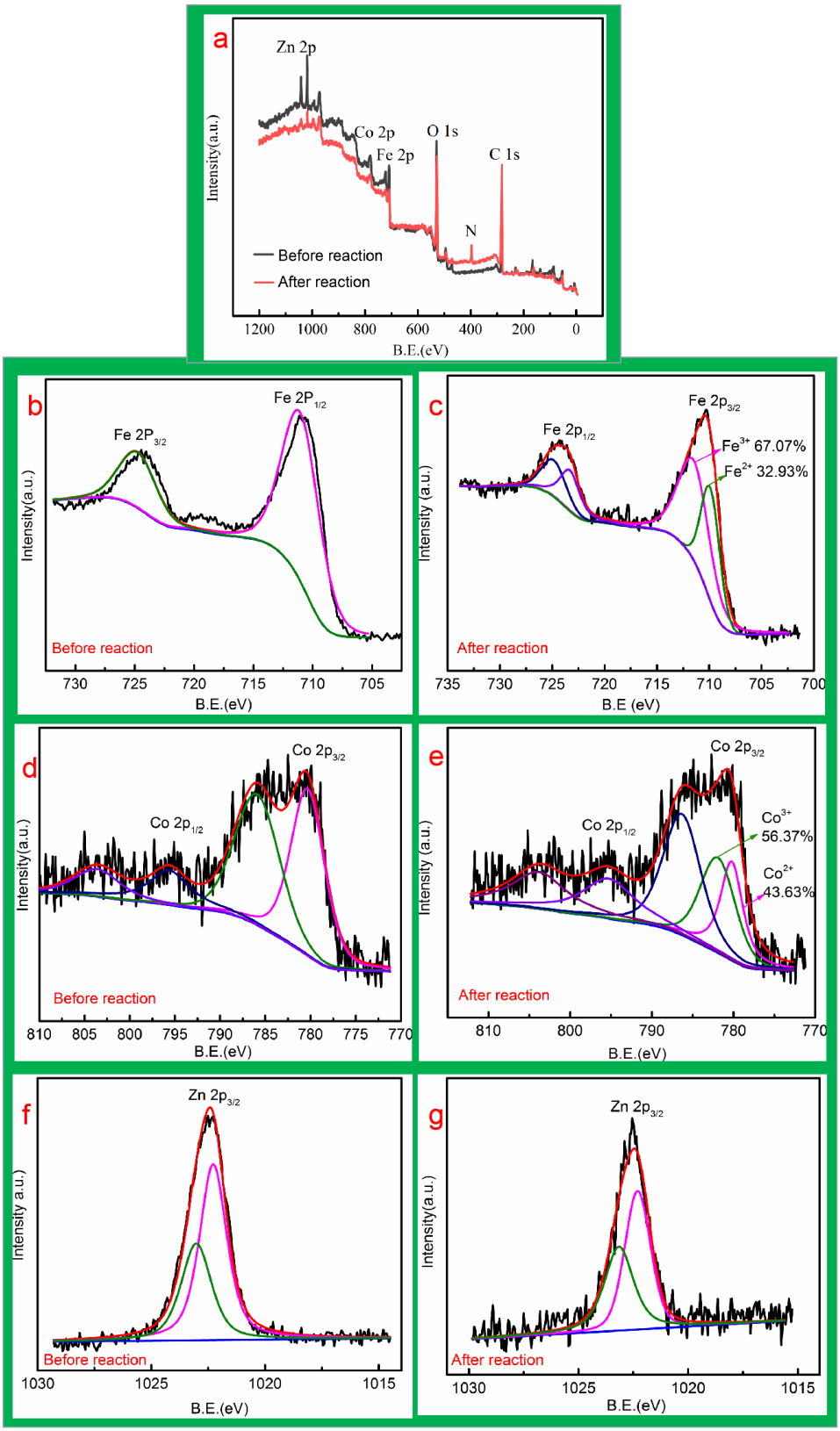

688

689 **Fig.21**. The XPS spectra of (a) wide-scan, (b) Co 2p (c) Fe 2p (d) O 1s of copper magnesium ferrite

690 nanoparticles.

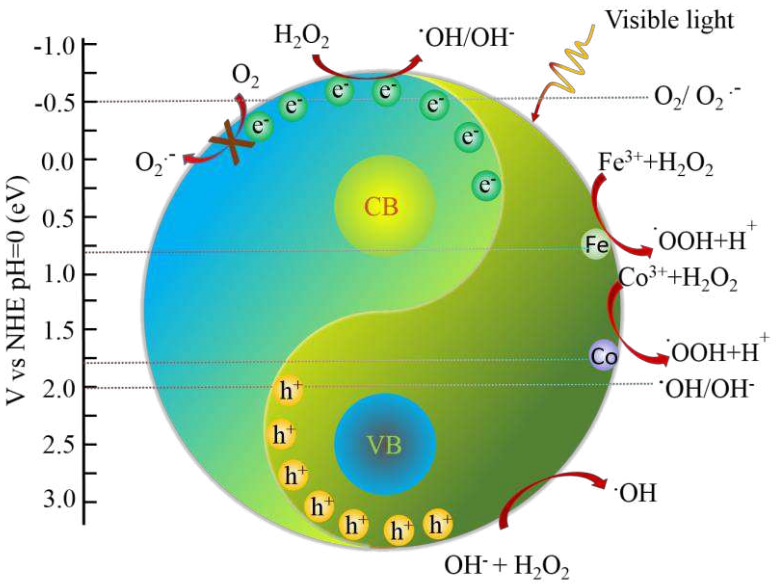

Fig.23. Schematic diagram of the degradation mechanism of $CoZnFeO_4$

3.5 MB intermediate and degradation pathway

At present, the research on photocatalytic degradation of dyes mainly focuses on the preparation of photocatalysts, the optimization of photocatalytic conditions, and reaction kinetics. While less attention is paid to the photocatalytic degradation mechanism of dye molecules [82]. Spadaro et al. [83] proposed that the photocatalytic degradation of dyes is mainly carried out by adding HO• to the carbon-nitrogen bond, and a series of unstable intermediates are formed and decomposed during the structural decomposition of dye chromophore [84]. Some intermediates may be more toxic than the parent molecule. Therefore, it is of great significance to determine the intermediates and whether there are intermediates that are difficult to be degraded.

MB is a kind of dye with a complex molecular structure. Its color is usually determined by the chromophobe group. This means that the decolorization of MB is caused by the destruction of chromogenic groups, but often the dye has not been

completely degraded, there are still a large number of toxic intermediates. To determine the degradation pathways and intermediates of MB, ion chromatography and ESI-MS are used for analysis (Fig. S24). As shown in Fig. 25, the anions in the solution are determined by ion chromatography, and the MB produced Cl^-, NO_3^- and SO_4^{2-} during the degradation process. The results showed that C-N, S-Cl, and C-S bonds are broken during the degradation of MB, thus Cl^-, NO_3^- and SO_4^{2-} are generated in the solution. To further determine the degradation pathway of MB, the degradation of products at different reaction times are identified by ESI-MS. As shown in Fig. 26, MB first deionized, S-Cl bond broke and Cl^- (m/z =284) is lost, and then HO• attacked C-S=C to generate sulfoxide (C-S(=O)-C) and $-NH_2$ fracture (m/z=303). The rest of the structure degrades in two ways, with the $-CH_3$ bond having the lowest energy and breaking first (m/z=270,256,281), Or $-CH_3$ is oxidized to HCHO on the surface of nucleophilic oxygen by chemical adsorption (m/z=332). Sulfoxide then breaks under the hydroxyl radical attack. The involvement of the two pathways in MB degradation depends on the competition between surface chemisorption and direct hydroxylation of MB [85]. Finally, under the action of hydrogen peroxide, MB is broken down into small molecules such as carbon dioxide and water.

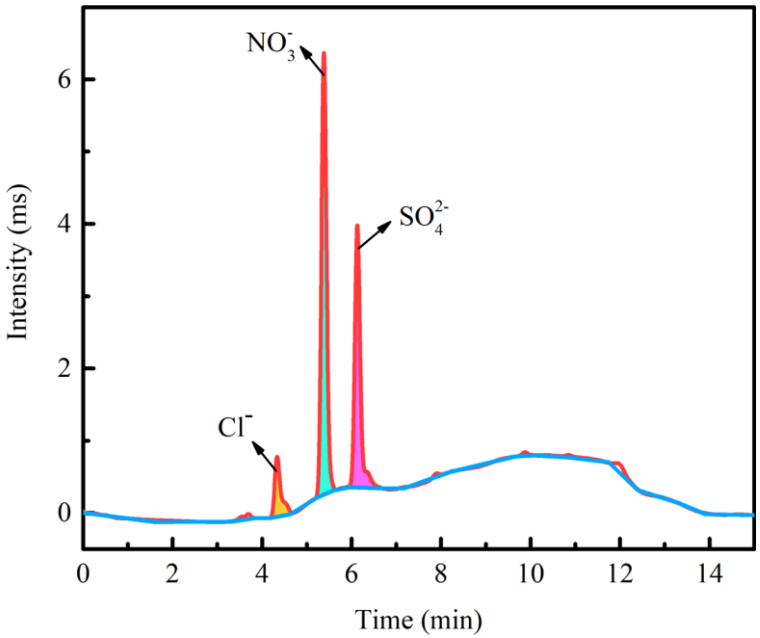

Fig.25. Ion chromatogram of reaction for 25min.

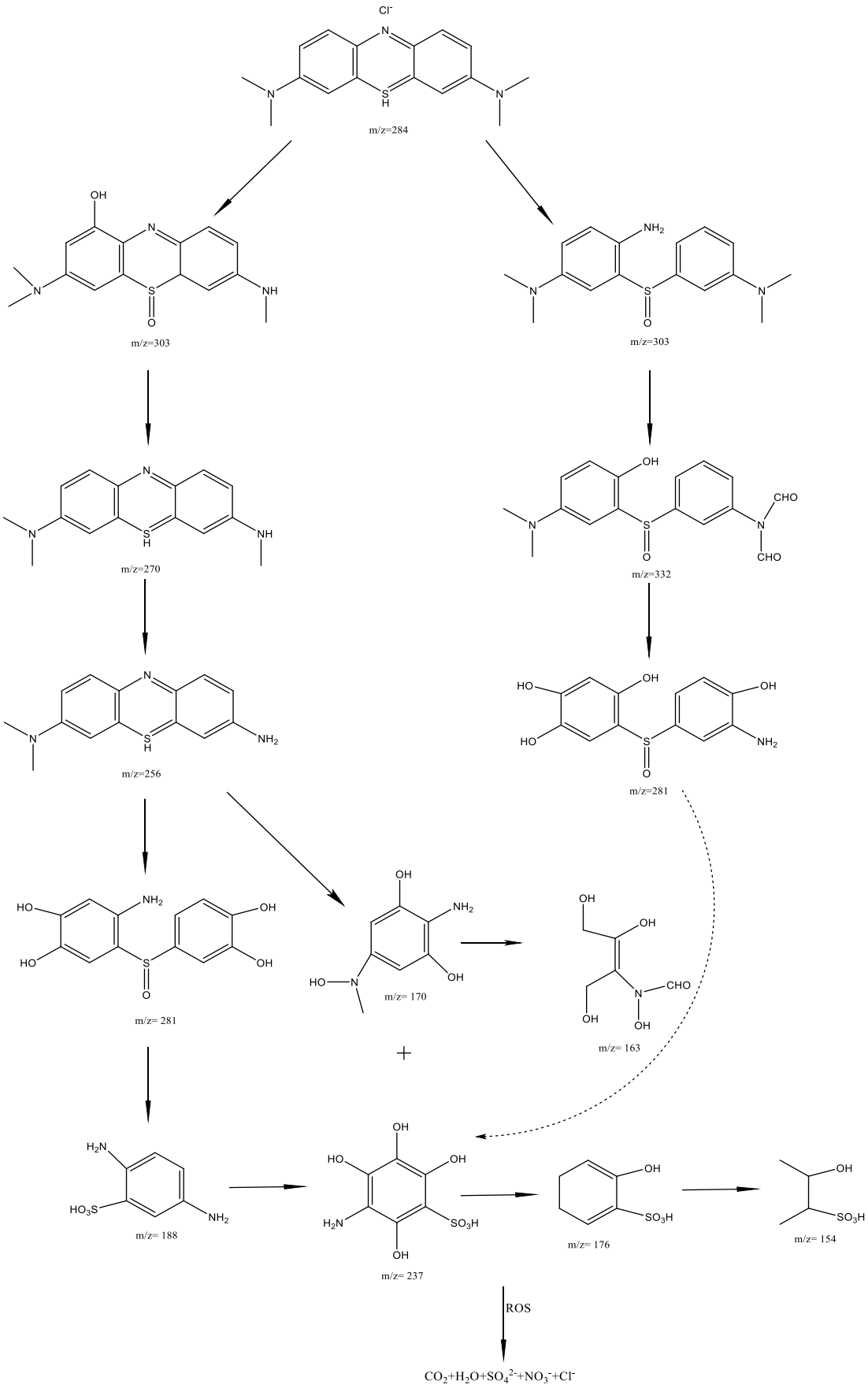

Fig.26. Methylene blue degradation pathway.

4 Conclusions

In this work, $CoZnFeO_4$ is synthesized by solid-phase method with titanium white waste residue as raw material, and the properties of the synthesized material are proved by XRD, FTIR and EDS. XPS tests show that cobalt is in the trivalent octahedral position of the spinel structure, which indicates that cobalt is substituted for iron in the synthesis. The BET test showed that Co^{3+} substitution with Fe^{3+} increased the specific surface area of the material, which greatly increased the active area of the catalyst, reduced the diffusion distance of photo-generated carriers, and improved the absorption efficiency of the material to light. By comparing the degradation of MB with different catalysts, it is found that $CoZnFeO_4$ had a better catalytic effect. In the discussion of the influence of pH, Zeta potential and ICP-MS proved that the main reason for the gradual decrease of decolorization rate with the increase of pH is the attraction of H_2O_2 by the charge of the catalyst particles. To produce hydroxyl radicals to complete the degradation of MB, while fewer metal ions extracted from the solution only played a role of auxiliary degradation. At the same time, the light wavelength, catalyst dosage, hydrogen peroxide concentration, MB concentration conditions are also explored, and through the comparison with other catalysts, it is proved that the catalyst synthesized in this work has high catalytic activity. After 5 cycles of use, $CoZnFeO_4$ can still maintain high catalytic activity, which proves that the structure of the material is stable. Through XPS analysis after the reaction, it is proved that cobalt and iron are the main factors in the whole catalytic process. The experiment of free radical capture shows that hydroxyl radical

and photogenic hole play a major role in the whole degradation process. The mechanism of the degradation process is analyzed with the aid of the forward molecular orbital theory. Finally, ion chromatography and ESI-MS are used to analyze the potential degradation pathways of MB. It shows that MB will eventually be completely degraded to non-toxic substances. The above reasons, determined that nanocatalysts synthesized from waste materials by one-step synthesis not only have the advantages of recycling but also can degrade organic matter effectively. This method of treating waste by waste can not only reduce the accumulation of industrial waste effectively but also expand the new thinking of treating wastewater

Declaration of Competing Interest

The authors declare that they have no known competing financial interests or personal relationships that could have appeared to influence the work reported in this paper.

Acknowledgments

This study is financially supported by Sichuan University-Panzhihua City Science and Technology Corporation Special Fund Project for Titanium White by-product Ferrous Sulfate Preparation 500 tons/year Nanometer iron Red Pigment and Co-production Sulfuric Acid Pilot Study Project (No. 2018CDPZH-5), and Sichuan Science and Technology Planning Project (No. 2019YFH0149).

References

[1] H. Zollinger, Color Chemistry: Synthesis, Properties and Applications of Organic Dyes and Pigments, Leonardo. 22 (1989) 313-314.doi:10.2307/1575449.

[2] A. Hassani, L. Alidokht, A.R. Khataee, S.Karaca, Optimization of comparative removal of two structurally different basic dyes using coal as a low-cost and available adsorbent, Journal of the Taiwan Institute of Chemical Engineers. 45 (2014) 1597-1607. doi:10.1016/j.jtice.2013.10.014.

[3] A. Hassani, R.D.C. Soltani, M. Kiransan, S.Kiransan, c.Karaca, A. Khataee, ltrasound-assisted adsorption of textile dyes using modified nanoclay: Central composite design optimization, Korean Journal of Chemical Engineering. 33(2016) 178-188. doi:10.1007/s11814-015-0106-y.

[4] C.H. Chen, Y.H. Liang, W.D. Zhang, $ZnFe_2O_4$/MWCNTs composite with enhanced photocatalytic activity under visible-light irradiation, Journal of Alloys & Compounds. (2010). doi:10.1016/j.jallcom.2010.04.072.

[5] W.F. Xui, X.J. Yuan, D.S. Xia, Preparation of Nanometer Zinc Ferrite and Its Application in Water Treatment, Technology of water treatment. 46 (2020). doi:10.16796/j.cnki.1000-3770.2020.07.002.

[6] T. Wu, G. Liu, J. Zhao, Photoassisted Degradation of Dye Pollutants. V. Self-Photosensitized Oxidative Transformation of Rhodamine B under Visible Light Irradiation in Aqueous TiO_2 Dispersions, The Journal of Physical Chemistry B.102(1998):5845-5851. doi:10.1021/jp980922c.

[7] A.B. Prevot, A. Basso, C. Baiocchi, M. Pazzi,G. Marci,V. Augugliaro, L. Palumisano, E. Pramauro, Analytical control of photocatalytic treatments: degradation of a sulfonated azo dye, Analytical and bioanalytical chemistry. 378 (2016) 214-20. doi:10.1007/s00216-003-2286-2.

[8] D.S. Nair, M. Kurian. Heterogeneous catalytic oxidation of persistent chlorinated organics over cobalt substituted zinc ferrite nanoparticles at mild conditions: Reaction kinetics and catalyst

reusability studies. Journal of Environmental Chemical Engineering, 2017, 5(2017) 964-974. doi: 10.1016/j.jece.2017.01.021.

[8] J.T. Spadaro, L. Isabelle, V. Renganathan. Hydroxyl radical-mediated degradation of azo dyes: evidence for benzene generation, Environmental ence & Technology. 28 (1994) 1389-93. doi:10.1021/es00056a031.

[9] C.H. Chen, Y.H. Liang, W.D. Zhang, $ZnFe_2O_4$/MWCNTs composite with enhanced photocatalytic activity under visible-light irradiation, Journal of Alloys & Compounds. (2010). doi:10.1016/j.jallcom.2010.04.072.

[10] R.M. Sharma, S. Bansal, S. Singhal, Tailoring the photo-Fenton activity of spinel ferrites (MFe_2O_4) by incorporating different cations (M = Cu, Zn, Ni and Co) in the structure, Rsc Advances. 2015. doi:10.1039/C4RA13692F.

[11] B. Sheng, Status and Development of Titanium Dioxide Industry in 2019, Iron Steel Vanadium Titanium.

[12] Y.L. Qiao, L. Ning, Development, Application, Research and Production of Titanium Dioxide in China, Chemical Industry and Engineering Progress. (1997).

[13] P. Brax, C. Burrage, Constraining Disformally Coupled Scalar Fields, Physical Review D. 90 (2014). doi:10.1103/PhysRevD.90.104009.

[14] A.B. Prevot, A. Basso, C. Baiocchi, M. Pazzi,G. Marci,V. Augugliaro, L. Palumisano, E. Pramauro, Analytical control of photocatalytic treatments: degradation of a sulfonated azo dye, Analytical and bioanalytical chemistry. 378 (2016) 214-20. doi:10.1007/s00216-003-2286-2.

[15] J.T. Spadaro, L. Isabelle, V. Renganathan. Hydroxyl radical-mediated dradation of azo dyes: evidence for benzene generation, Environmental ence & Technology. 28 (1994) 1389-93. doi:10.1021/es00056a031.

[16] L. Wolski, M. Ziolek, Insight into pathways of methylene blue degradation with H_2O_2 over mono and bimetallic Nb, Zn oxides, Applied Catalysis, B. Environmental: An International Journal Devoted to Catalytic ence and Its Applications. 2018, 224 (2018) 634-647. doi.org/10.1016/j.apcatb.2017.11.008.

[17] D.S. Nair, M. Kurian. Heterogeneous catalytic oxidation of persistent chlorinated organics over cobalt substituted zinc ferrite nanoparticles at mild conditions: Reaction kinetics and catalyst reusability studies, Journal of Environmental Chemical Engineering. 5 (2017) 964-974. doi:10.1016/j.jece.2017.01.021.

[18] L. Chen, D.H. Ding, C. Liu, H. Cai. Y. Qu, S.J. Yang, Y. Gao, T.M. Cai, Decolorization of norfloxacin by $CoFe_2O_4$-GO composite coupled with peroxymonosulfate: A comparative study and mechanistic consideration, Chemical Engineering Journal. 2018. doi:10.1016/j.cej.2017.10.040.

[19] S.D. Li, H.S. Wang, W.M. Li, X.F. Wu, W.X. Tang, Y.F. Chen, Effect of Cu substitution on promoted benzene oxidation over porous CuCo-based catalysts derived from layered double hydroxide with resistance of water vapor, Applied Catalysis B Environmental. 166-167 (2015) 260-269. doi: 10.1016/j.apcatb.2014.11.040.

[20] S.J. Gregg, K.S.W. Sing, Adsorption, Surface Area and Porosity (Academic, London,1982). doi:10.1524/zpch.1969.63.1_4.220.

[21] D.S. Nair, M. Kurian, Heterogeneous catalytic oxidation of persistent chlorinated organics

over cobalt substituted zinc ferrite nanoparticles at mild conditions: Reaction kinetics and catalyst reusability studies, Journal of Environmental Chemical Engineering. 5 (2017) 964-974. doi: 10.1016/j.jece.2017.01.021.

[22] P.D. Yang, D.Y. Zhao, D.I. Margolese, B.F. Chmelka, G.D. Stucky, Generalized syntheses of large-pore mesoporous metal oxides with semicrystalline frameworks, Nature. 396 (1998) 152-155. doi: 10.1038/24132.

[23] Y.J. Yao, G.D.Wu, F. Lu, S.B. Wang, Y. Hu, J. Zhang, W.Z. Huang, F.Y. Wei, Enhanced photo-Fenton-like process over Z-scheme $CoFe_2O_4$/g-C_3N_4 Heterostructures under natural indoor light. Environmental ence & Pollution Research, 2016. doi: 10.1007/s11356-016-7329-2.

[24] M. Sundararajan, V. Sailaja, L.J. Kennedy, J.J.Vijaya, Photocatalytic Decolorization of rhodamine B under visible light using nanostructured zinc doped cobalt ferrite: kinetics and mechanism, Ceramics International. 43(2017). doi:10.1016/j.ceramint.2016.09.191.

[25] D.F. Zhang, F.B. Zeng, Visible light-activated cadmium-doped ZnO nanostructured photocatalyst for the treatment of methylene blue dye, Journal of Materials ence. 47 (2012) 2155-2161. doi:10.1007/s10853-011-6016-4.

[26] S. Asuha, B. Suyala, S. Zhao, Porous structure and Cr(VI) removal abilities of Fe_3O_4 prepared from Fe–urea complex, Materials Chemistry & Physics. 129 (2011) 483-487. doi:10.1016/j.matchemphys.2011.04.044.

[27] A. Zielińska-Jurek, B. Zuzanna, D. Szymon. Design and Application of Magnetic Photocatalysts for Water Treatment. The Effect of Particle Charge on Surface Functionality, Catalysts. 7 (2017) 360. doi:10.3390/catal7120360.

[29] M. Kosmulski, C. Saneluta, Point of zero charge/isoelectric point of exotic oxides: Tl_2O_3, J. Colloid Interface Sci. 280 (2004) 544–545. doi:10.1016/j.jcis.2004.08.079.

[30] A. Augustine, A. Pius, Photocatalytic degradation of monocrotophos and chlorpyrifos in aqueous solution using TiO_2 under UV radiation, Journal of Water Process Engineering. (2015). doi:10.1016/j.jwpe.2015.06.002.

[31] H..H. Yang, B.F. Shi, S.L. Wang. Fe Oxides Loaded on Carbon Cloth by Hydrothermal Process as an Effective and Reusable Heterogenous Fenton Catalyst, Catalysts. 8 (2018) 207. doi:10.3390/catal8050207.

[32] A. Augustine, A. Pius, Photocatalytic degradation of monocrotophos and chlorpyrifos in aqueous solution using TiO_2 under UV radiation, Journal of Water Process Engineering. (2015). doi:10.1016/j.jwpe.2015.06.002.

[33] Y.N. Zhou, Y.G. Wang, T. Wen, S.Y. Zhang, B.B. Chang, Y.Z. Guo, B.C.Yang, Mesoporous Cd1-xZnxS microspheres with tunable bandgap and high specific surface areas for enhanced visible-light-driven hydrogen generation, Journal of Colloid and Interface Science. (2016). doi: 10.1016/j.jcis.2016.01.003.

[34] M. Chandrika, A.V. Ravindra, C. Rajesh, S.D. Ramarao, S.H.Tu, Studies on structural and optical properties of nano $ZnFe_2O_4$ and $ZnFe_2O_4$-TiO_2 composite synthesized by Co-precipitation route, Materials Chemistry and Physics. 230 (2019) 107-113. doi: 10.1016/j.matchemphys.2019.03.059.

[35] W. Chu, W.K. Choy, The mechanisms of rate enhancing and quenching of trichloroethene photodecay in the presence of sensitizer and hydrogen sources, Water Research. 36 (2002) 2525-2532. doi:10.1016/S0043-1354(01)00471-7.

[36] D.F. Ollis, E. Pelizzetti, N. Serpone, Destruction of Water Contaminants, Environmental ence & Technology. 25 (1991). doi: 10.1021/es00021a001.

[37] D.F. Ollis, E. Pelizzetti, N. Serpone, Destruction of Water Contaminants, Environmental ence & Technology. 25 (1991). doi: 10.1021/es00021a001.

[38] I. Ilisz, K. Foglein, Dombi, A. J. Mol. Catal. 135 (1998) 55.

[39] R.M. Gao, J. Stark, D.W. Bahnemann, J. Rabani, Quantum yields of hydroxyl radicals in illuminated TiO_2 nanocrystallite layers.148 (2002) 387-391. doi: 10.1016/s1010-6030(02)00066-7.

[40] X.F. Xue, K. Hanna, M. Abdelmoula, N.S. Deng, Adsorption and oxidation of PCP on the surface of magnetite: Kinetic experiments and spectroscopic investigations, Applied Catalysis B Environmental, 89 (2009) 432-440. doi: 10.1016/j.apcatb.2008.12.024.

[41] S.X. Zha, Y. Cheng, Y. Gao, Z.L. Chen, M. Megharej, R. Naidu, Nanoscale zero-valent iron as a catalyst for heterogeneous Fenton oxidation of amoxicillin, Chemical Engineering Journal. 255 (2014) 141-148. doi: 10.1016/j.cej.2014.06.057.

[42] R.A. Doong, W.H. Chang, Photodegradation of Parathion in Aqueous Titanium Dioxide and Zero Valent Iron Solutions in the Presence of Hydrogen Peroxide, Journal of Photochemistry and Photobiology A Chemistry. 116 (1998) 221-228. doi: 10.1016/S1010-6030(98)00292-5.

[43] Y.J. Yao, G.D. Wu, F.Lu, S.B.Wang. Y.Hu, J.Zhang, H.Z.Huang, F.Y.Wei. En-hanced photo-Fenton-like process over Z-scheme $CoFe_2O_4$/g-C_3N_4 Heterostructur-es under natural indoor light, Environmental Science & Pollution Research, 2016. doi: 10.1007/s11356-016-7329-2.

[44] R.M. Sharma, S. Bansal, S. Singhal, Tailoring the photo-Fenton activity of spinel ferrites (MFe_2O_4) by incorporating different cations (M = Cu, Zn, Ni and Co) in the structure, Rsc Advances. 2015. doi:10.1039/C4RA13692F.

[45] Z.Q. He, C. Gao, M.Q. Qian, Y.Q. Shi, J.M. Chen, S. Song, Electro-Fenton Process Catalyzed by Fe_3O_4 Magnetic Nanoparticles for Decolorization of C.I. Reactive Blue 19 in Aqueous Solution: Operating Conditions, Influence, and Mechanism, Ind. Eng. Chem. Res. 53 (2014) 3435−3447. doi:/10.1021/ie403947b.

[46] T.R. Gordon, A.L. Marsh, Temperature Dependence of the Oxidation of 2-Chlorophenol by Hydrogen Peroxide in the Presence of Goethite, Catalysis Letters, 132 (2009) 349-354. doi: 10.1007/s10562-009-0125-6.

[47] H.Y. Xu, M. Prasad, Y. Liu. Schorl: A novel catalyst in mineral-catalyzed Fenton-like system for dyeing wastewater discoloration, Journal of Hazardous Materials. 165 (2009) 1186-1192. doi: 10.1016/j.jhazmat.2008.10.108.

[48] Q.Liao, J. Sun, L. Gao, Decolorization of phenol by heterogeneous Fenton reaction using multi-walled carbon nanotube supported Fe_2O_3 Catalysts, Colloid Surf. A-Physicochem. Eng. Asp. 345 (2009) 95-100. doi: 10.1016/j.colsurfa.2009.04.037.

[49] J.H. Sun, S.P. Sun, G.L. Wang, L.P. Qiao. Decolorization of azo dye Amido black 10B in aqueous solution by Fenton oxidation process, Dyes & Pigments. 74 (2007) 647-652. doi: 10.1016/j.dyepig.2006.04.006.

[50] F.J. Millero, S. Sotolongo, The oxidation of Fe (II) with H_2O_2 in seawater, Geochimica Et Cosmochimica Acta. 53 (1989) 1867-1873. doi:10.1016/0016-7037(89)90307-4.

[51] S.P. Sun, C.J. Li, J.H. Sun, S.H. Shi, M.H. Fan, Q.Zhan, Decolorization of an azo dye Orange G in aqueous solution by Fenton oxidation process: Effect of system parameters and kinetic study, Journal of Hazardous Materials.161 (2009) 1052-1057. doi:10.1016/j.jhazmat.2008.04.080.

[52] S.D. Khairhal, V.S. Shrivastava, Photocatalytic Decolorization of chlorpyrifos and methylene blue using α-Bi_2O_3 nanoparticles fabricated bysolgel method. 1 (2019). doi: 10.1007/s42452-019-0761-4.

[53] S. Jauhar, S. Singhal, Manganese substituted cobalt ferrites as efficient catalysts for H_2O_2 assisted Decolorization of cationic and anionic dyes: Their synthesis and characterization. (2014) doi: 10.1016/j.apcata.2014.08.020.

[54] S. F. Chen, W. Zhao, W. Liu, H.Y. Zhang, X.L. Yu, Y.H. Chen, Preparation, characterization and activity evaluation of p-n junction photocatalyst-$CaFe_2O_4$n-ZnO, Chem. Eng. J. 155 (2009) 466–473. doi: 10.1016/j.jhazmat.2009.08.007.

[55] S. Chen, W. Zhao, W. Liu, H. Zhang, X. Yu, Y. Chen, Preparation, characterization and activity evaluation of p-n junction photocatalyst p$CaFe_2O_4$/n-Ag_3VO_4 under visible light irradiation, J. Hazard. Mater. 172 (2009) 1415–1423.

[56] C.H. Chen, Y.H. Lian, W.D. Zhang, $ZnFe_2O_4$/MWCNTs composite with enhanced photocatalytic activity under visible-light irradiation, Journal of Alloys & Compounds. (2010) doi: 10.1016/j.jallcom.2010.04.072.

[57] R.C.C. Costa, M.D.F.F. Lelis, L.C.A. Oliveira, J.D. Fabvis, J.D. Ardisson, R.R.r.A.Rios, C.N. Silva, R.M. Lago, Remarkable effect of Co and Mn on the activity of Fe_xM_xO promoted oxidation of organic contaminants in aqueous medium with HO, Catalysis Communications. 4 (2003) 525-529. doi:10.1016/j.catcom.2003.08.002.

[58] C.H. Bartholomew, Mechanisms of catalyst deactivation, 212 (2001) 17-60. doi: 10.1016/s0926-860x(00)00843-7.

[59] P. Forzatti, L. Lietti. Catalyst deactivation. Catalysis Today. 52 (199) 165-181. doi:

10.1016/S0920-5861(99)00074-7.

[60] S. Choudhary, A. Bisht, S. Mohapatra, Facile synthesis, morphological, structural, photocatalytic and optical properties of $CoFe_2O_4$ nanostructures. 2019. doi: 10.1007/s42452-019-1665-z.

[61] M. Felaez, P. Falaras, V. Likodinos. K.Shea, A. Armah, D.L. Cruz, P.S.M. Dunlop, Use of selected scavengers for the determination of NF-TiO_2 reactive oxygen species during the decolorization of microcystin-LR under visible light irradiation, Journal of Molecular Catalysis A Chemistry. (2016). doi:10.1016/j.molcata.2016.09.035.

[62] C.C. Chen, X.Z. Li, W.H. Ma, J.C.Zhao, Effect of Transition Metal Ions on the TiO_2-Assisted PhotoDecolorization of Dyes under Visible Irradiation: A Probe for the Interfacial Electron Transfer Process and Reaction Mechanism, Journal of Physical Chemistry B. 106 (2002) 318-324. doi: 10.1021/jp0119025.

[63] Q. Liu, Y.R. Guo, Z.H. Chen, Z.G. Zhang, X.M. Fang, Constructing a novel ternary Fe(III)/graphene/g-C_3N_4, composite photocatalyst with enhanced visible-light-driven photocatalytic activity via interfacial charge transfer effect, Applied Catalysis B Environmental. 83 (2016) 231-241. doi.org/10.1016/j.apcatb.2015.10.054

[64] N.P. Devi, M. Maisnam, Characterizations of Sol-Gel Synthesized and High Energy Ball Milled Spinel Nanoferrites: MFe_2O_4 (M=Li, Ni, Zn, Mn) for Nanofluid Preparations, Integrated Ferroelectrics. 204 (2020) 133-141. doi: 10.1080/10584587.2019.1674972.

[65] A.K. Srivastava, M. Deepa, N. Bahadur, M.S. Groyat, Influence of Fe doping on nanostructures and photoluminescence of sol-gel derived ZnO, Materials Chemistry & Physics. 114 (2008) 194-198. doi: 10.1016/j.matchemphys.2008.09.005.

[66] A. Manikandan, J.J. Manikandan, M. Sundararajan, M.Bououdina, Optical and magnetic properties of Mg-doped $ZnFe_2O_4$ nanoparticles prepared by rapid microwave combustion method, Superlattices & Microstructures. 64 (2013). doi: 10.1016/j.spmi.2013.09.021.

[67] G.J. Srinet, R. Kumar, V. Sajal, Effects of aluminum doping on structural and photoluminescence properties of ZnO nanoparticles, Ceramics International. 40 (2014) 4025-4031. doi: 10.1016/j.ceramint.2013.08.055.

[68] B.J. Rani, M. Ravina, B, Saravanakumar, G.Rari, V. Ganesh, S.Ravichandran, R. Yurakkumar, Ferrimagnetism in cobalt ferrite ($CoFe_2O_4$) nanoparticles. 14 (2018) 84-91. doi: 10.1016/j.nanoso.2018.01.012.

[69] D.D. Dionysiou, M.T. Suidan, I, Baudim, J.M. Laine, Effect of hydrogen peroxide on the destruction of organic contaminants-synergism and inhibition in a continuous-mode photocatalytic reactor, Applied Catalysis B: Environmental. 50 (2004) 259-269. doi: 10.1016/S0926-3373(04)00087-6.

[70] Y. Xing, Y.Y. Yin, J.C. Si, M.L.Peng, X.F. Wang, C.Chen, Y.L.Cui, Controllable synthesis and characterization of Fe_3O_4/Au composite nanoparticles, Journal of Magnetism and Magnetic Materials. (2015). doi: 10.1016/j.jmmm.2014.09.060.

[71] A. Khataee, M. Taseidifar, S. Khorram, M. Sheydaei, Preparation of nanostructured magnetite with plasma for Decolorization of a cationic textile dye by the heterogeneous Fenton process, Journal of the Taiwan Institute of Chemical Engineers. (2015). doi: 10.1016/j.jtice.2015.02.023.

[72] Y. Lei, C.S. Chen, Y.J. Tu, Y.H. Zhang, Heterogeneous Decolorization of Organic Pollutants by Persulfate Activated by CuO-Fe_3O_4: Mechanism, Stability, and Effects of pH and Bicarbonate Ions, Environmental ence & Technology. 49 (2015) 6838-6845. doi: 10.1021/acs.est.5b00623.

[73] Y.J. Yao, G.D. Wu, F. Lu, S.B. Wang, Y. Hu, J. Zhang, W.Z. Huang, F. Wei, Enhanced photo-Fenton-like process over Z-scheme $CoFe_2O_4$/g-C_3N_4 Heterostructures under natural indoor light[J]. Environmental ence & Pollution Research. (2016). doi: 10.1007/s11356-016-7329-2.

[74] M. Li, Y.P. Xiong, X.T. Liu, X.J. Zhang, C. Han, L.P. Guo, Facile synthesis of electrospun MFe_2O_4 (M = Co, Ni, Cu, Mn) spinel nanofibers with excellent electrocatalytic properties for oxygen evolution and hydrogen peroxide reduction, Nanoscale. 7 (2015) 8920-8930. doi: 10.1039/C4NR07243J.

[75] B. Cai, M.G. Zhao, Y. Ma, Z.Z.Ye, J.Y.Huang, Bioinspired Formation of 3D Hierarchical $CoFe_2O_4$ Porous Microspheres for Magnetic-Controlled Drug Release, Acs Applied Materials & Interfaces.(2015). doi:10.1021/am507689a.

[76] L. Lou, A.E. Nelson, G. Heo, P.W. Major, Surface chemical composition of human maxillary first premolar as assessed by X-ray photoelectron spectroscopy (XPS), Applied Surface ence. 254 (2008) 6706-6709. doi: 10.1016/j.apsusc.2008.04.085.

[77] J.D. Li, Y.B. Li, L. Zhang, Y.Zuo, Composition of calcium-deficient Na-containing carbonate hydroxyapatite modified with Cu(II) and Zn(II) ions.

[78] G.X. Huang, C.Y. Huang, C.W, Yang, P.C. Guo, H.Q. Yu, Decolorization of Bisphenol A by Peroxymonosulfate Catalytically Activated with Mn1.8Fe1.2O4 Nanospheres: Synergism between Mn and Fe, Environmental ence & Technology. 51 (2017) 12611-12618. doi: 10.1021/acs.est.7b03007.

[79] A.S. Albuquerque, M.V.C. Tolentino, J.D. Ardisson, F.C.C. Mouraet, R.D. Mendenca, W.A.A. Macedo, Nanostructured ferrites: Structural analysis and catalytic activity, Ceramics International. 38 (2012) 2225-2231. doi: 10.1016/j.ceramint.2011.10.071.

[80] S. Lu, G.L. Wang, S. Chen, H.T. Yu, F. Ye, X.Quan, Heterogeneous activation of peroxymonosulfate by $LaCo_1$-xCu_xO_3 perovskites for Decolorization of organic pollutants, Journal of Hazardous Materials. 353 (2018) 401. doi: 10.1016/j.jhazmat.2018.04.021.

[81] C.X. Yang, W.P. Dong, G.W. Cui, Y.Q. Zhao, X.F.Shi, X.Y. Xia, B.Tang, W.L. Wang, Highly efficient photocatalytic Decolorization of methylene blue by P2ABSA-modified TiO_2 nanocomposite due to the photosensitization synergetic effect of TiO_2 and P_2ABSA, RSC Advances. doi: 10.1039/C7RA02423A.

[82] A.L. Linsebigler, G. Lu, J.T.Y. Lu, Photocatalysis on TiO_2 Surfaces: Principles, Mechanisms, and Selected Results, Chemical Reviews.95 (1995) 735-758.

[83] A.B. Prevot, A. Basso, C. Baiocchi, M. Pazzi,G. Marci,V. Augugliaro, L. Palumisano, E. Pramauro, Analytical control of photocatalytic treatments: degradation of a sulfonated azo dye, Analytical and bioanalytical chemistry. 378 (2016) 214-20. doi:10.1007/s00216-003-2286-2.

[84] J.T. Spadaro, L. Isabelle, V. Renganathan. Hydroxyl radical-mediated dradation of azo dyes: evidence for benzene generation, Environmental ence & Technology. 28 (1994) 1389-93. doi:10.1021/es00056a031.

[85] L. Wolski, M. Ziolek, Insight into pathways of methylene blue degradation with H_2O_2 over mono and bimetallic Nb, Zn oxides, Applied Catalysis, B. Environmental: An International Journal Devoted to Catalytic ence and Its Applications. 224 (2018) 634-647. doi.org/10.1016/j.apcatb.2017.11.008.

Figures

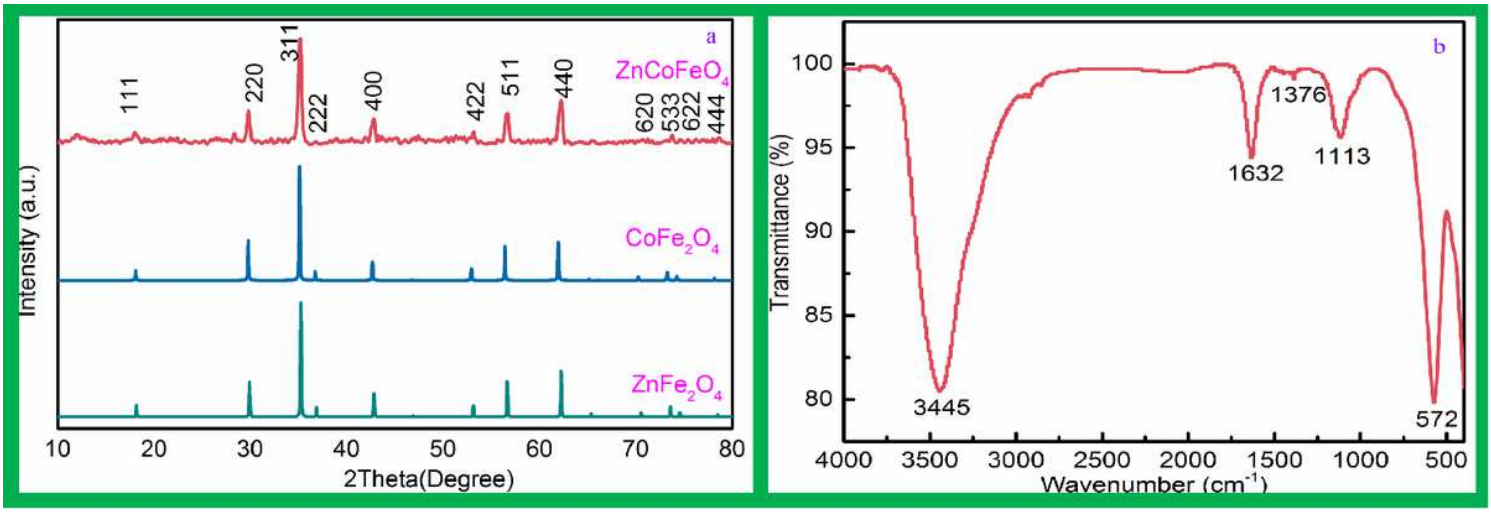

Figure 1

(a) the XRD patterns, (b) FTIR spectrum of copper magnesium ferrite nanoparticles

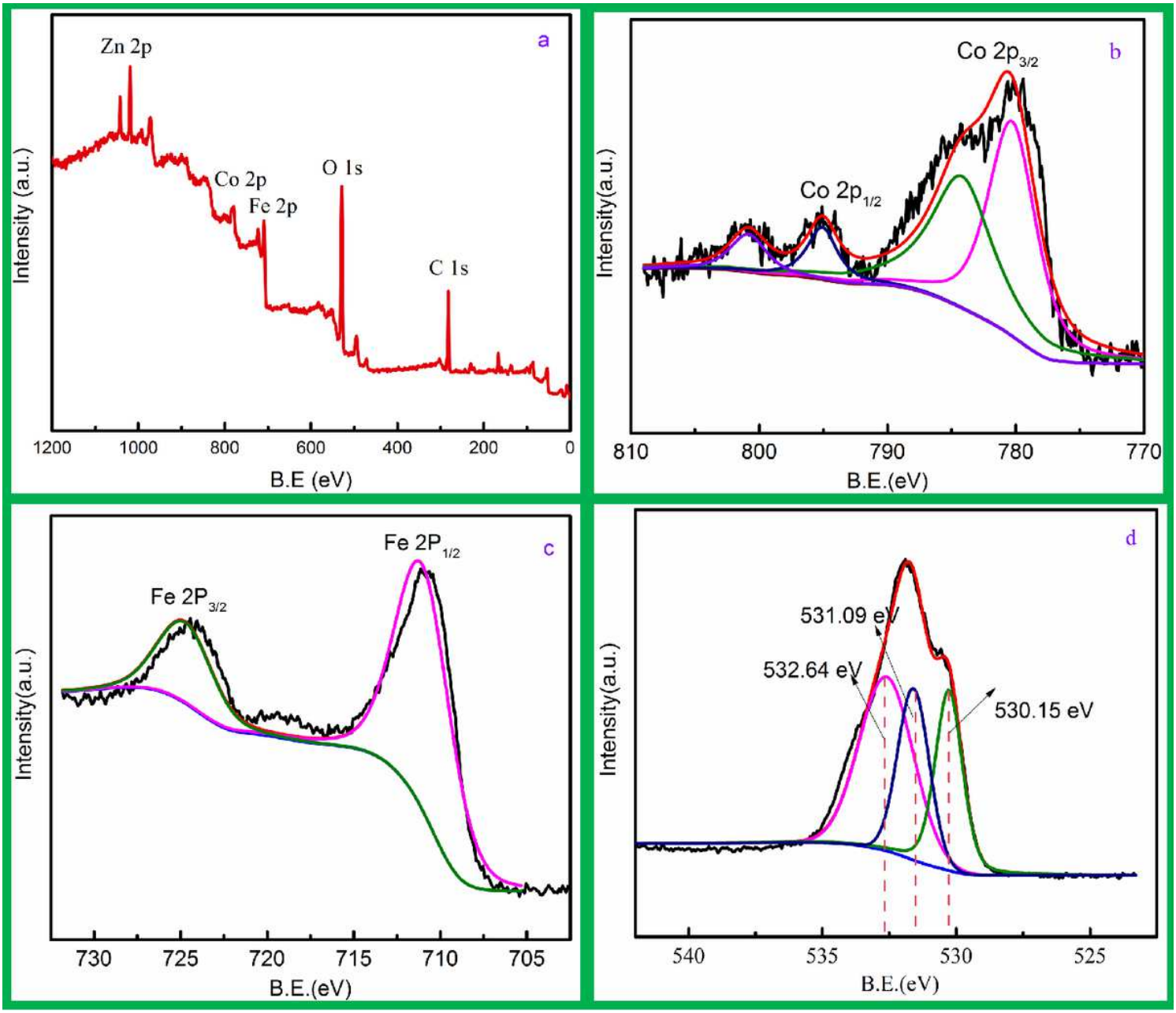

Figure 2

The XPS spectra of (a) wide-scan, (b) Co 2p (c) Fe 2p (d) O 1s of copper magnesium ferrite nanoparticle.

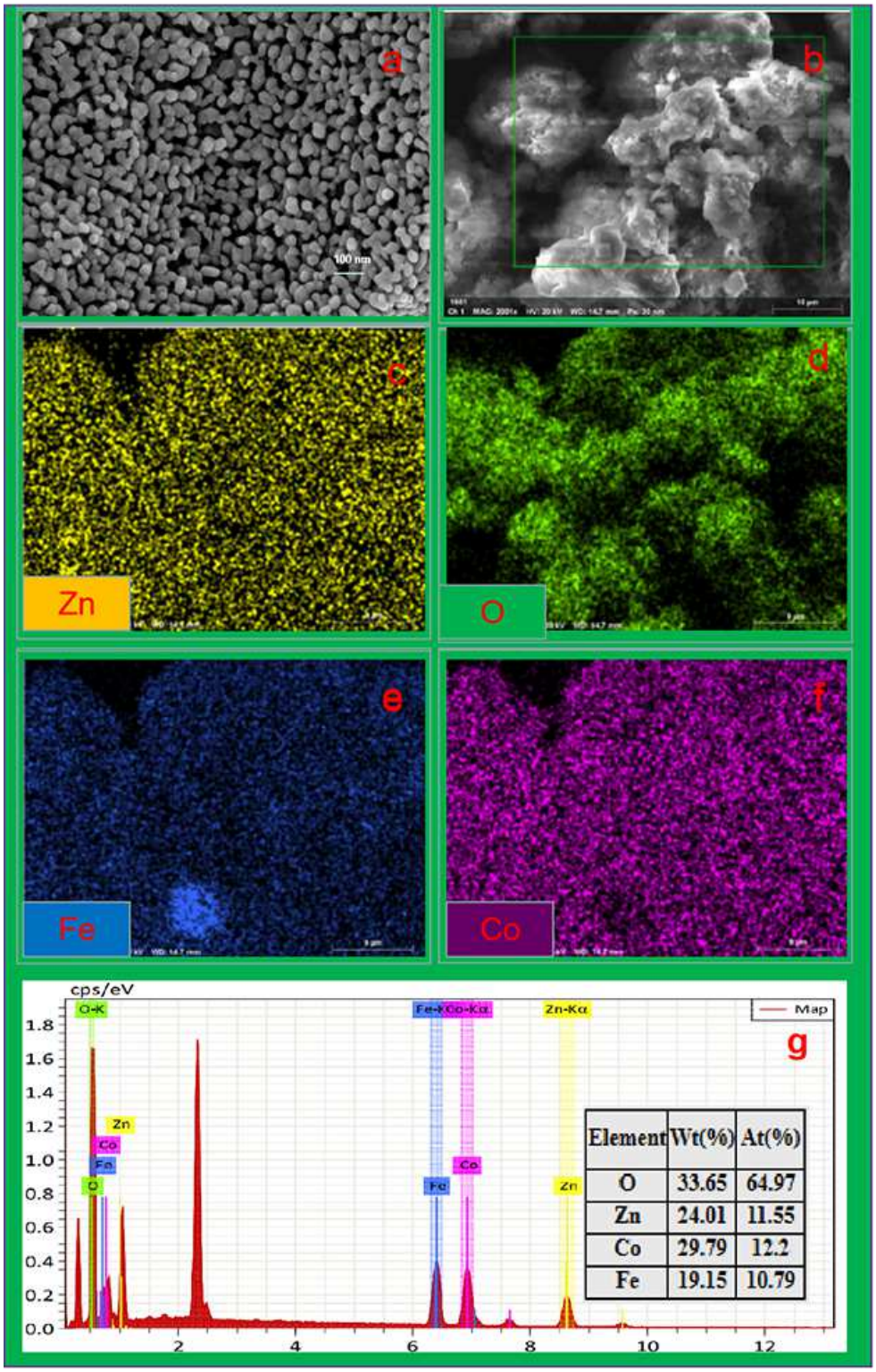

Figure 3

(a) the SEM image, (b-f) EDS patterns of copper magnesium ferrite nanoparticles

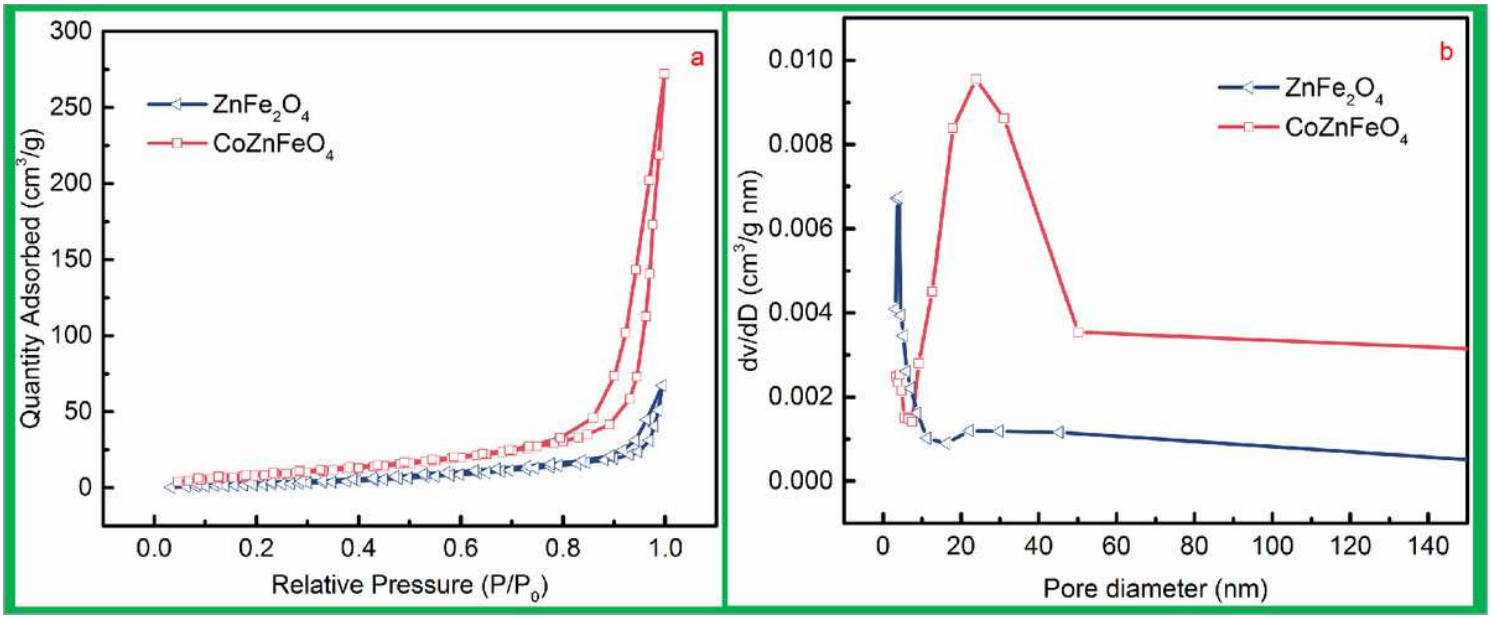

Figure 4

(a) N2 adsorption/desorption isotherms, and (b) Pore size distribution curves of the CoZnFeO4 and ZnFe2O4 spinel oxides.

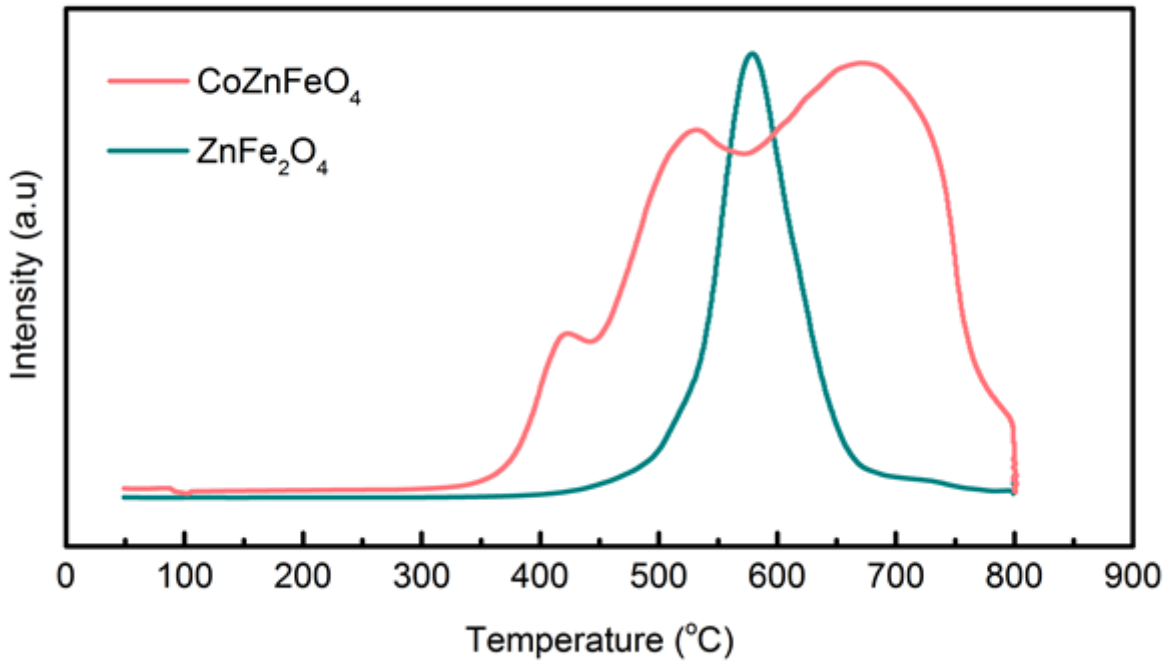

Figure 5

H2-TPR Profile of CoZnFeO4 and ZnFe2O4 nanocomposites

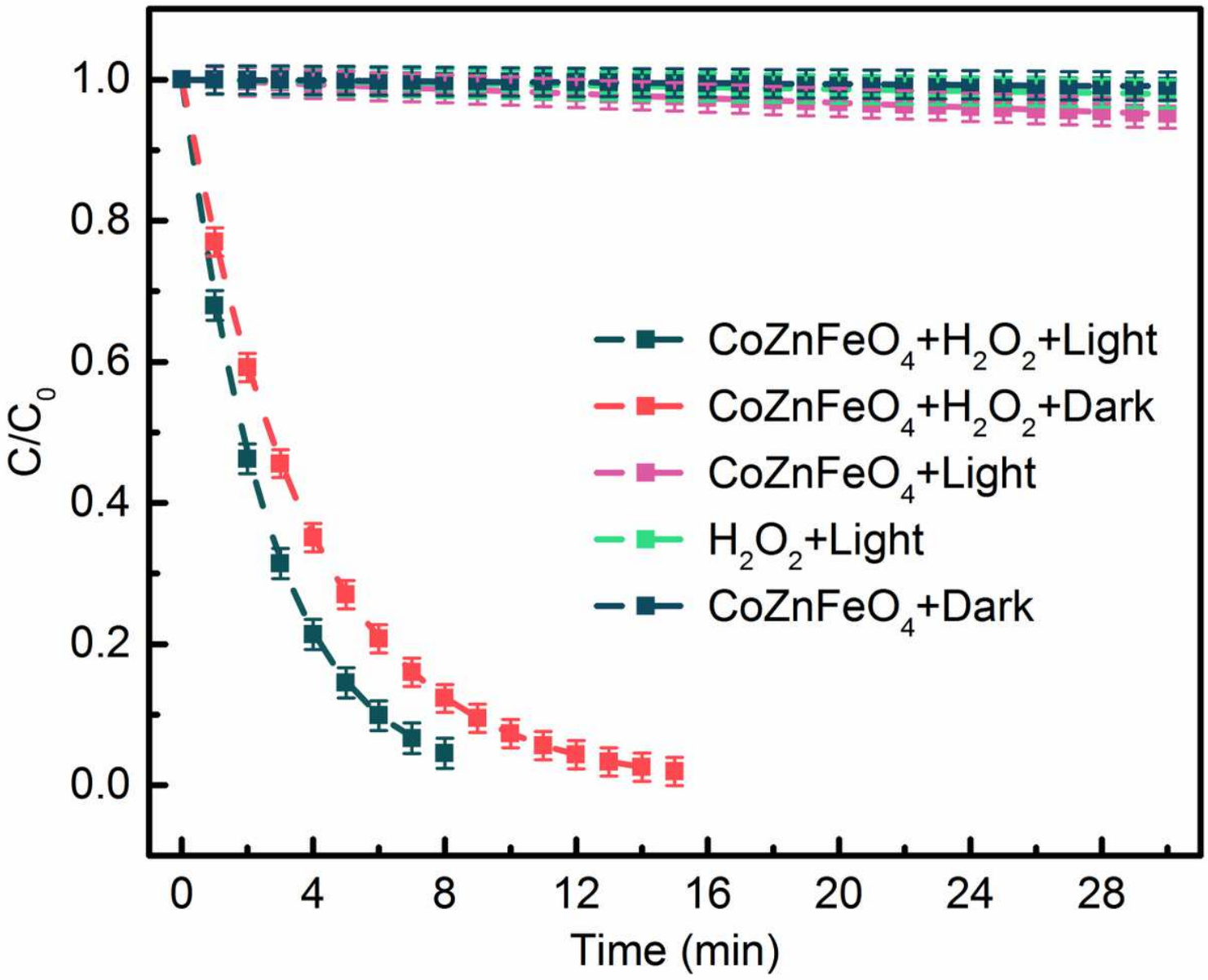

Figure 6

Decolorization rate of MB in different systems. Conditions: solid-to-liquid ratio = 1:500, MB = 200 mg/L, H2O2 = 20 mM/L, wavelength = 395 nm, T = 298 K.

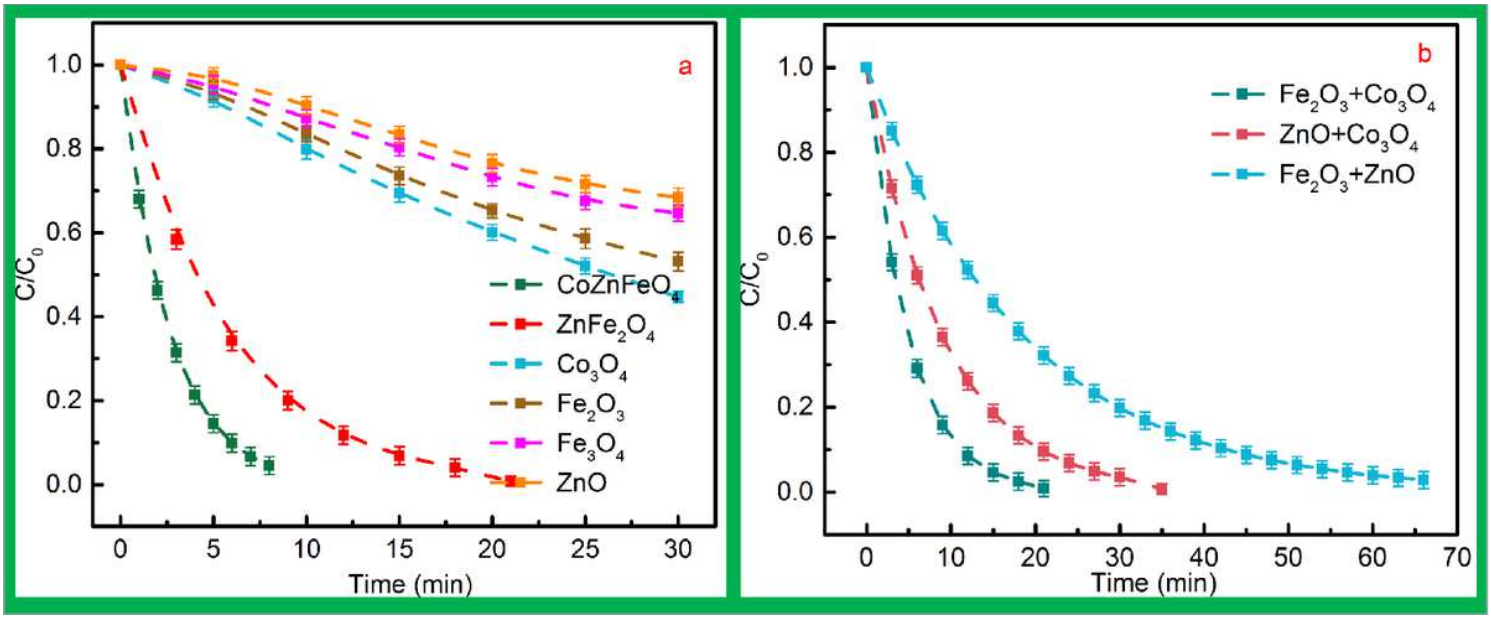

Figure 7

(a)Effect of different catalysts on MB decolorization; (b)Effects of different metal ion combinations on MB decolorization. Conditions: solid-to-liquid ratio = 1:500, MB = 200 mg/L, H2O2 = 20 mM/L, wavelength = 395 nm, T = 298 K.

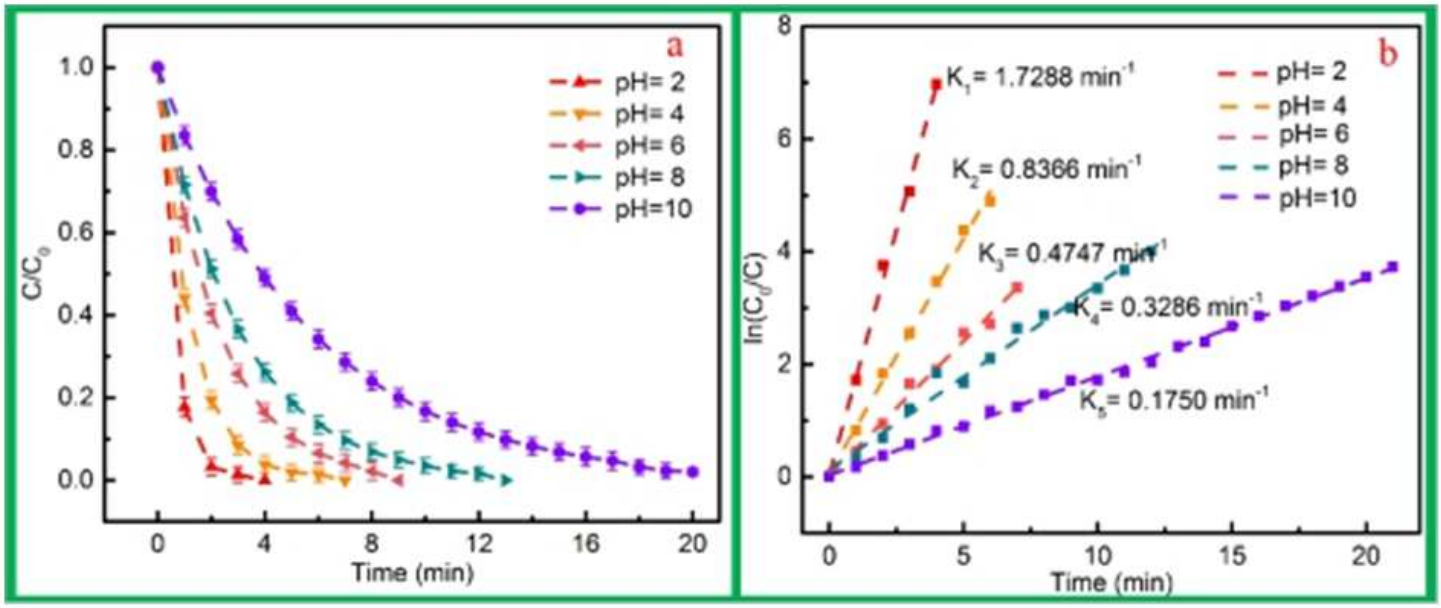

Figure 8

(a) Effect of pH on decolorization rate of MB, (b) Effect of pH on decolorization rate of MB. Conditions: solid-to-liquid ratio = 1:500, MB = 200 mg/L, H2O2 = 20 mM/L, wavelength = 395 nm, T = 298 K.

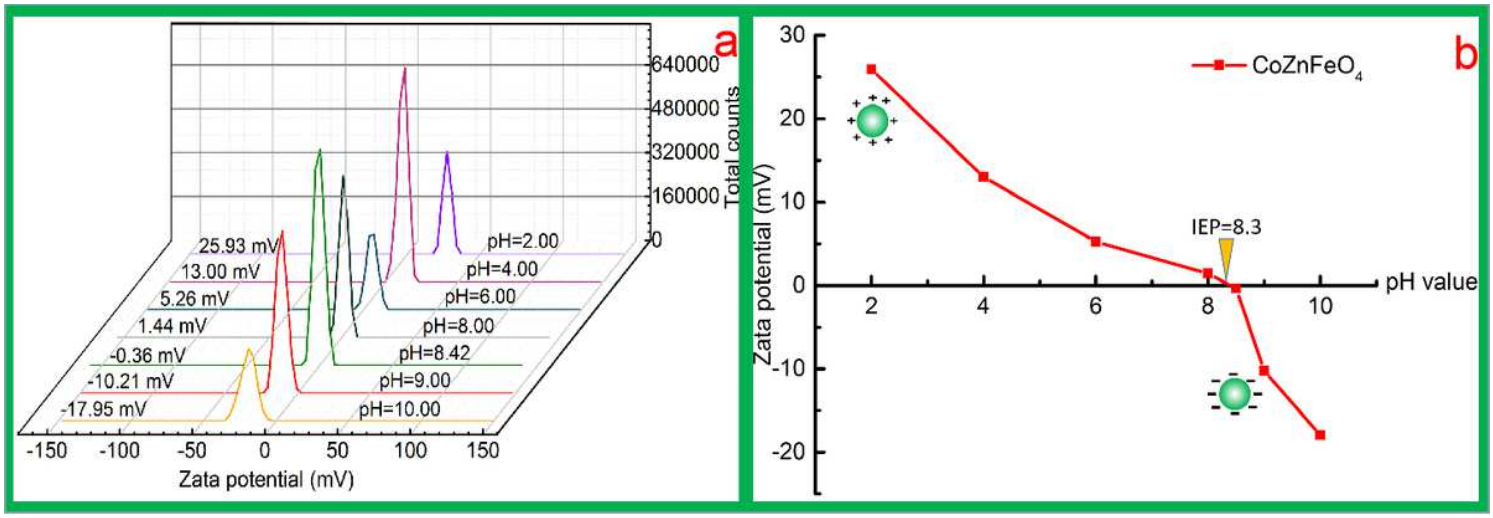

Figure 9

(a) Under different PH conditions, the potential of CoZnFeO4 nanoparticles is easured by Marvin instrument; (b) Zeta potential of CoZnFeO4 nanoparticles as a function of pH.

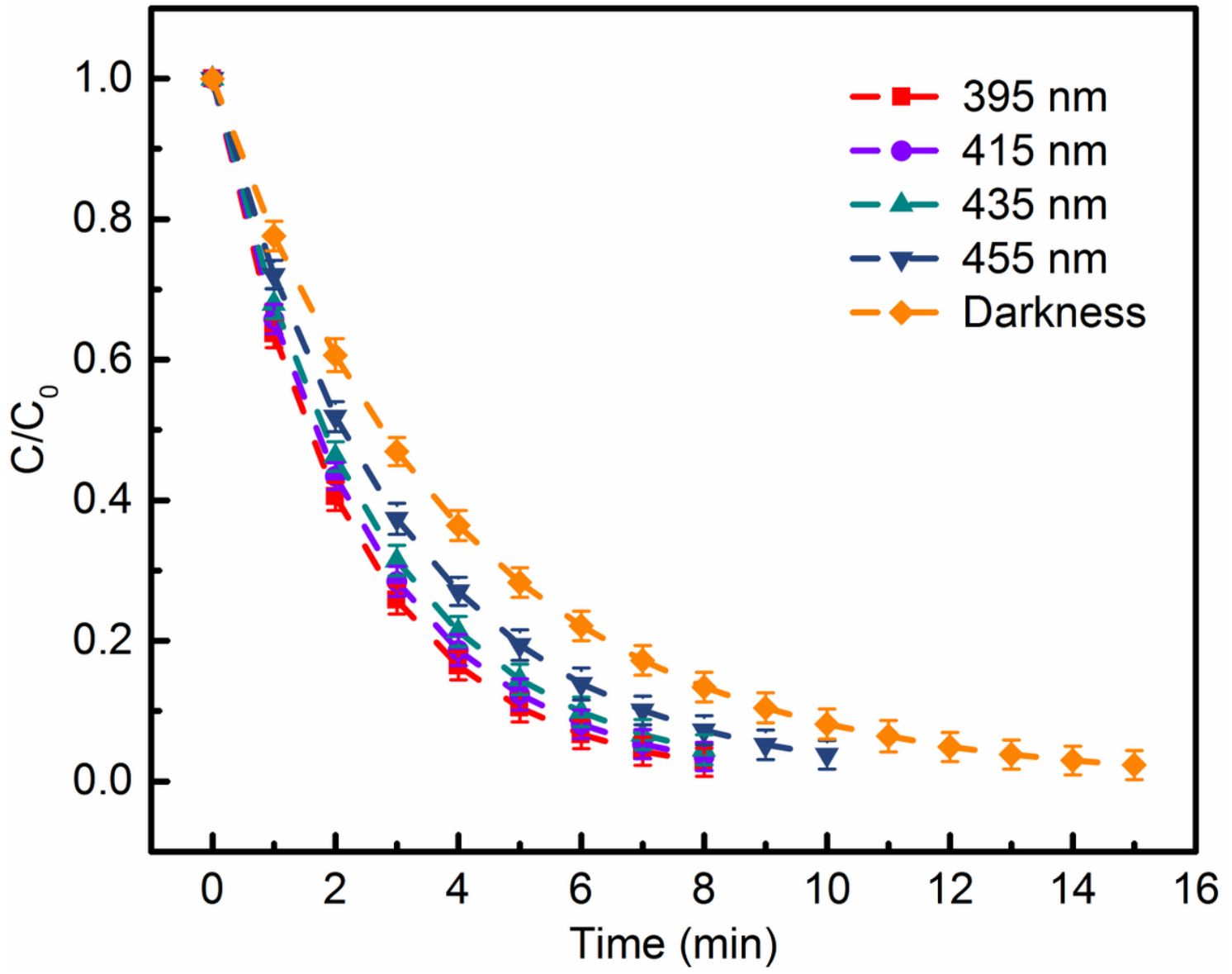

Figure 10

Effect of the wavelength on the decolorization of MB. Conditions: solid-to-liquid ratio = 1:500, MB = 200 mg/L, H2O2 = 20 mM/L, wavelength = 395 nm, T = 298 K.

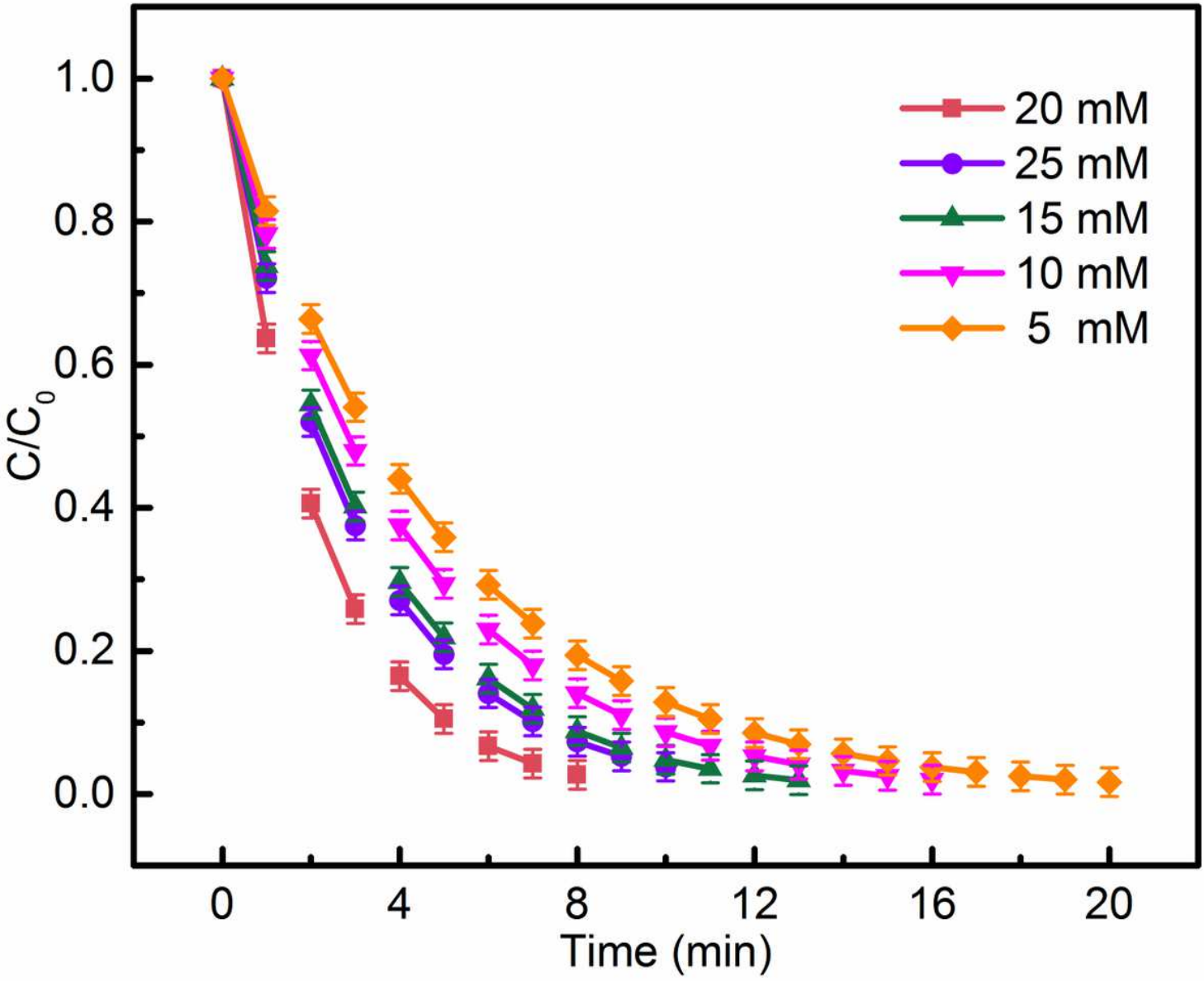

Figure 11

Effect of hydrogen peroxide concentration on the decolorization rate of MB. Conditions: solid-to-liquid ratio = 1:500, MB = 200 mg/L, H2O2 = 20 mM/L, wavelength = 395 nm, T = 298K.

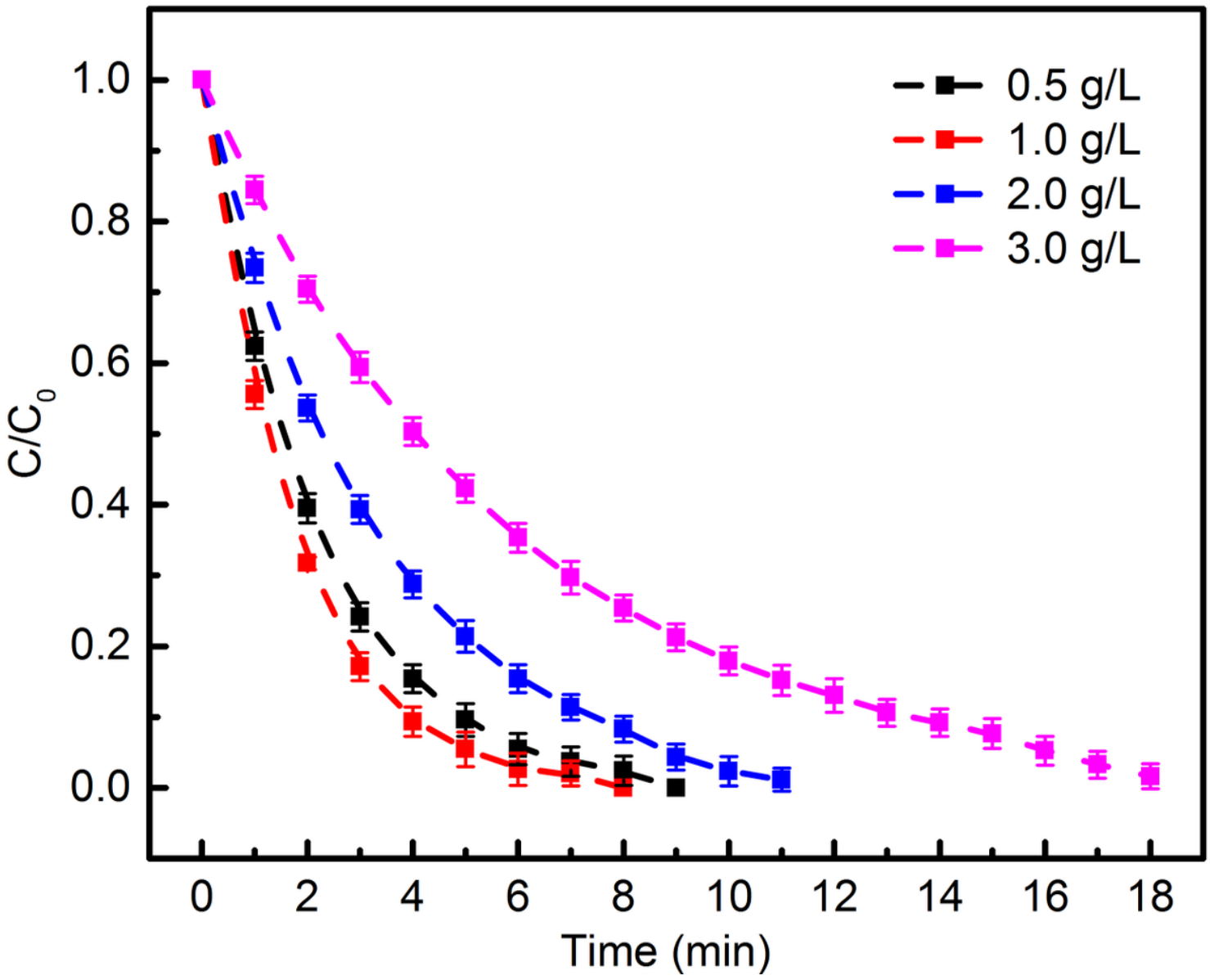

Figure 12

Effect of catalyst dosage on the decolorization of MB.Conditions: wavelength = 395 nm, H2O2 = 20 mM/L, T = 298 K.

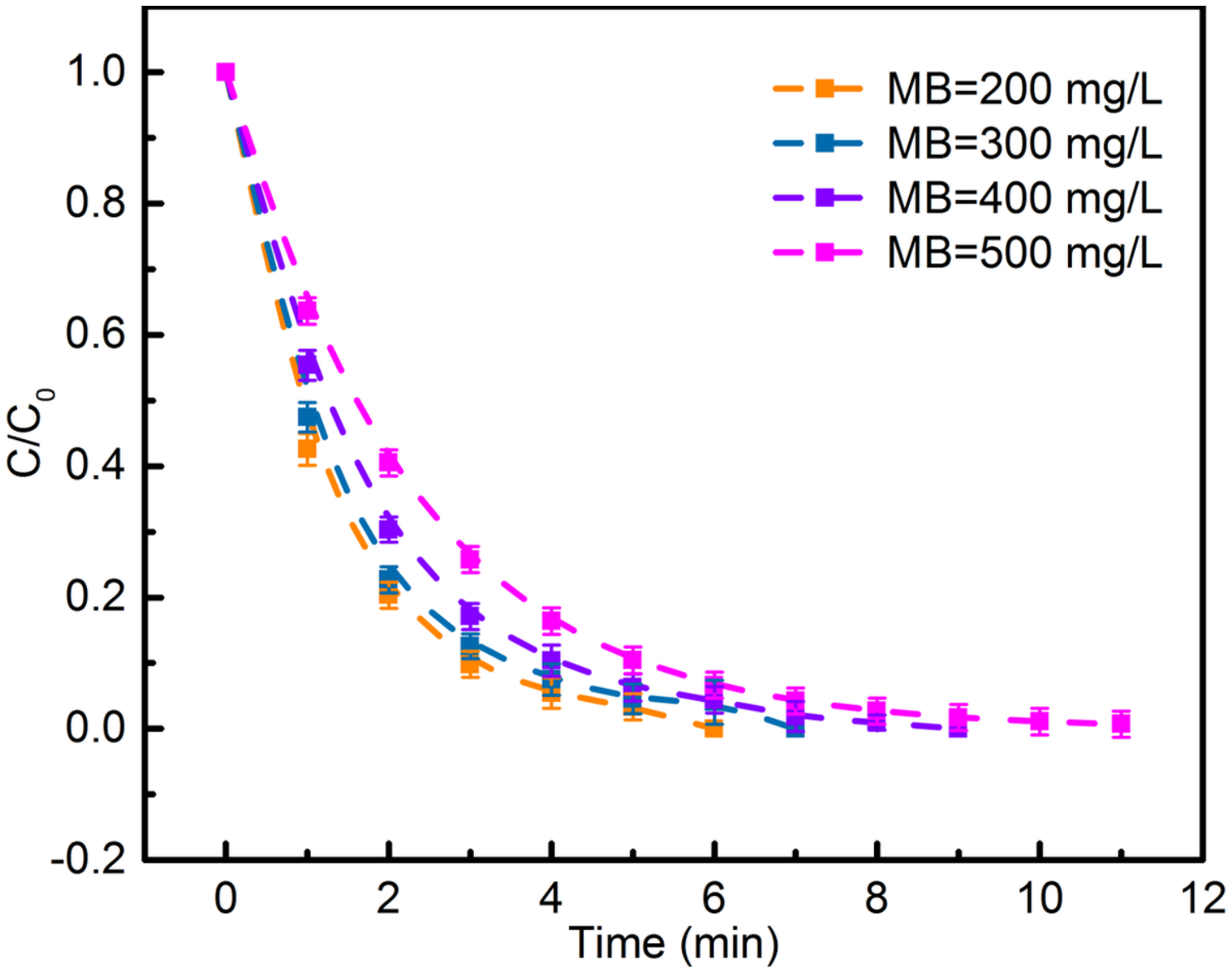

Figure 13

Effect of MB concentration on decolorization rate. Conditions: wavelength = 395 nm, solid-to-liquid ratio = 1:1000, T = 298 K.

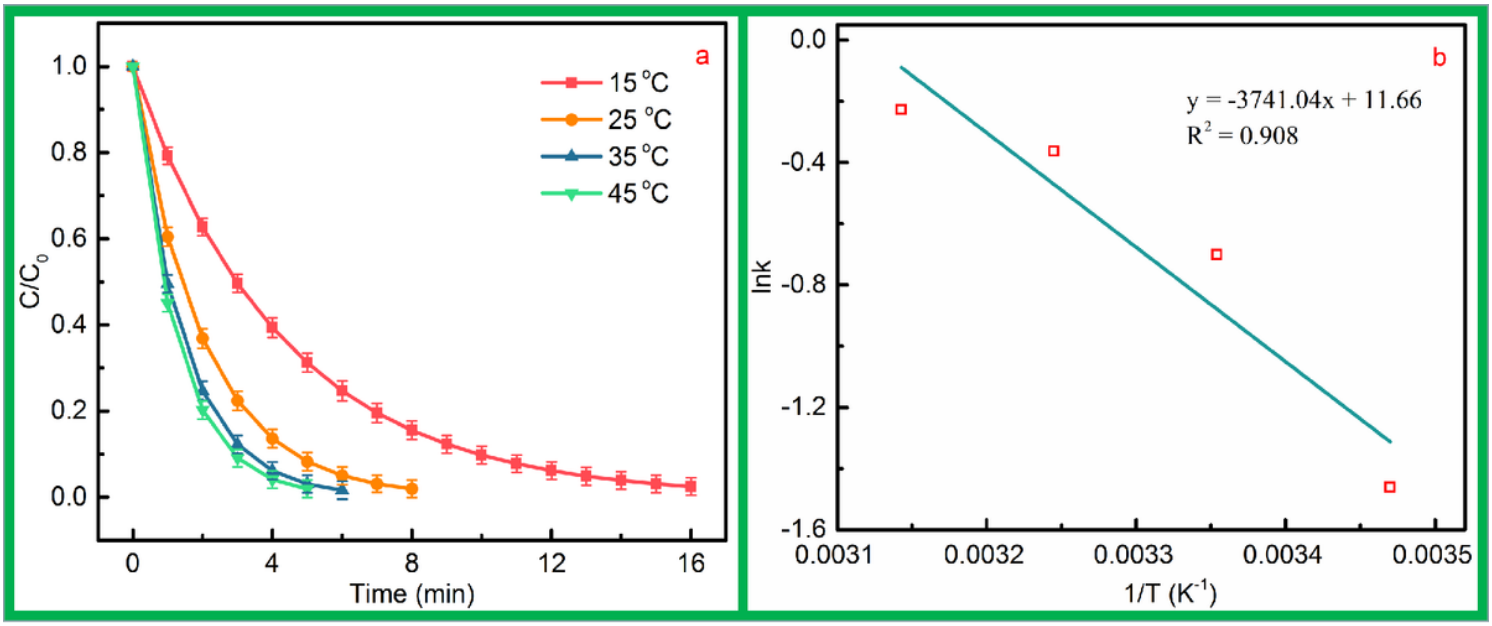

Figure 14

(a) Effect of temperature on the catalytic performance of CoZnFeO4, (b) the Arrhenius plot of lnk versus 1/T of the decolorization of MB by photocatalytic. Conditions: solid-to-liquid ratio = 1:1000, MB = 200 mg/L, H2O2 =20 mM/L, wavelength: 395 nm.

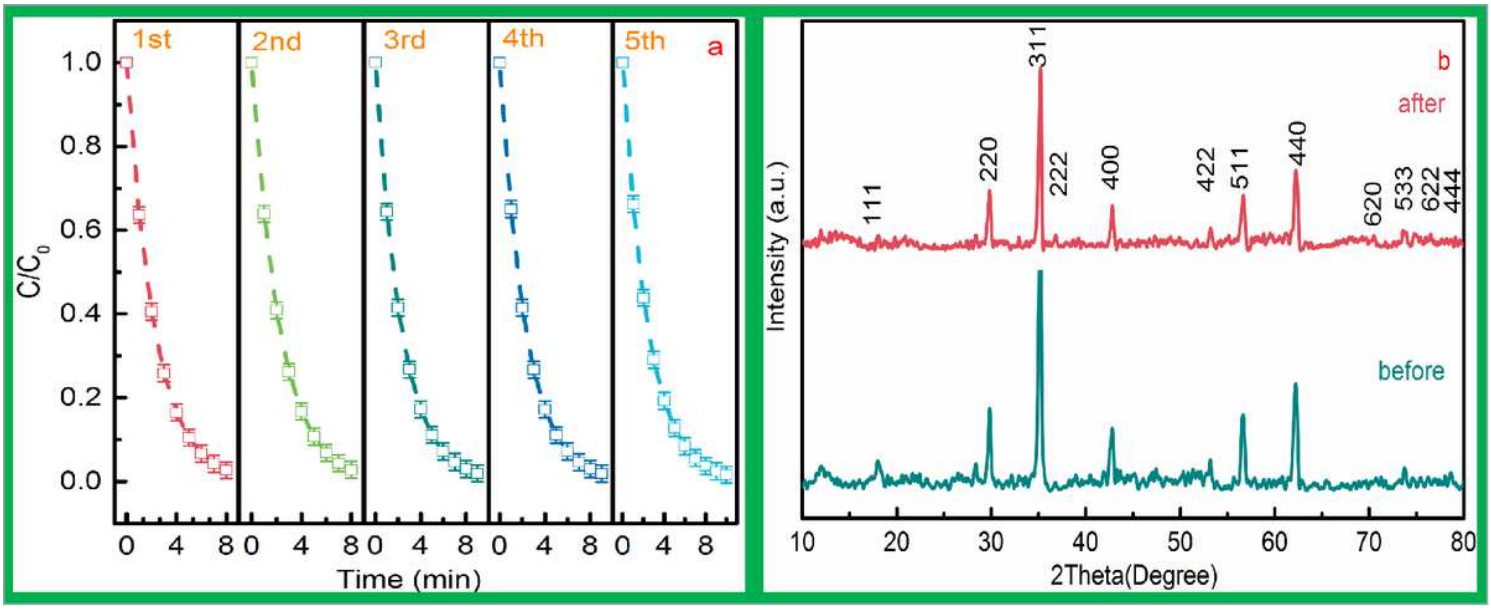

Figure 15

The reusability of CoZnFeO4 for MB decolorization in the presence of light (a); XRD patterns of CoZnFeO4 before and after the reaction (b). Conditions: solid-to-liquid ratio = 1:1000, MB = 200 mg/L, H2O2 = 20 mM/L, wave=length = 395 nm, T = 300.15 K.

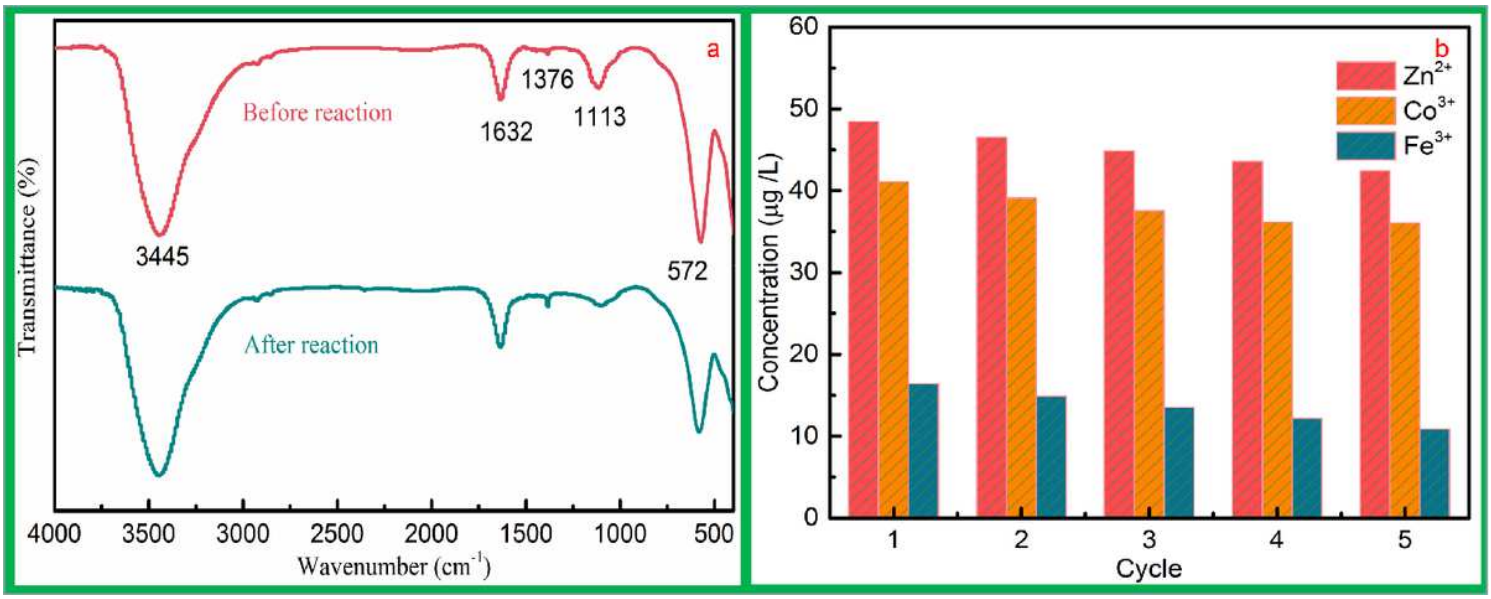

Figure 16

FTIR patterns of CoZnFeO4 before and after the reaction (a); The leaching amount of Zn2+, Co3+ and Fe3+ after cyclic decolorization of CoZnFeO4 for 5 times (b). Conditions: solid-to-liquid ratio = 1:1000, MB = 200 mg/L, H2O2 = 20 mM/L, wavelength = 395 nm, T = 300.15 K.

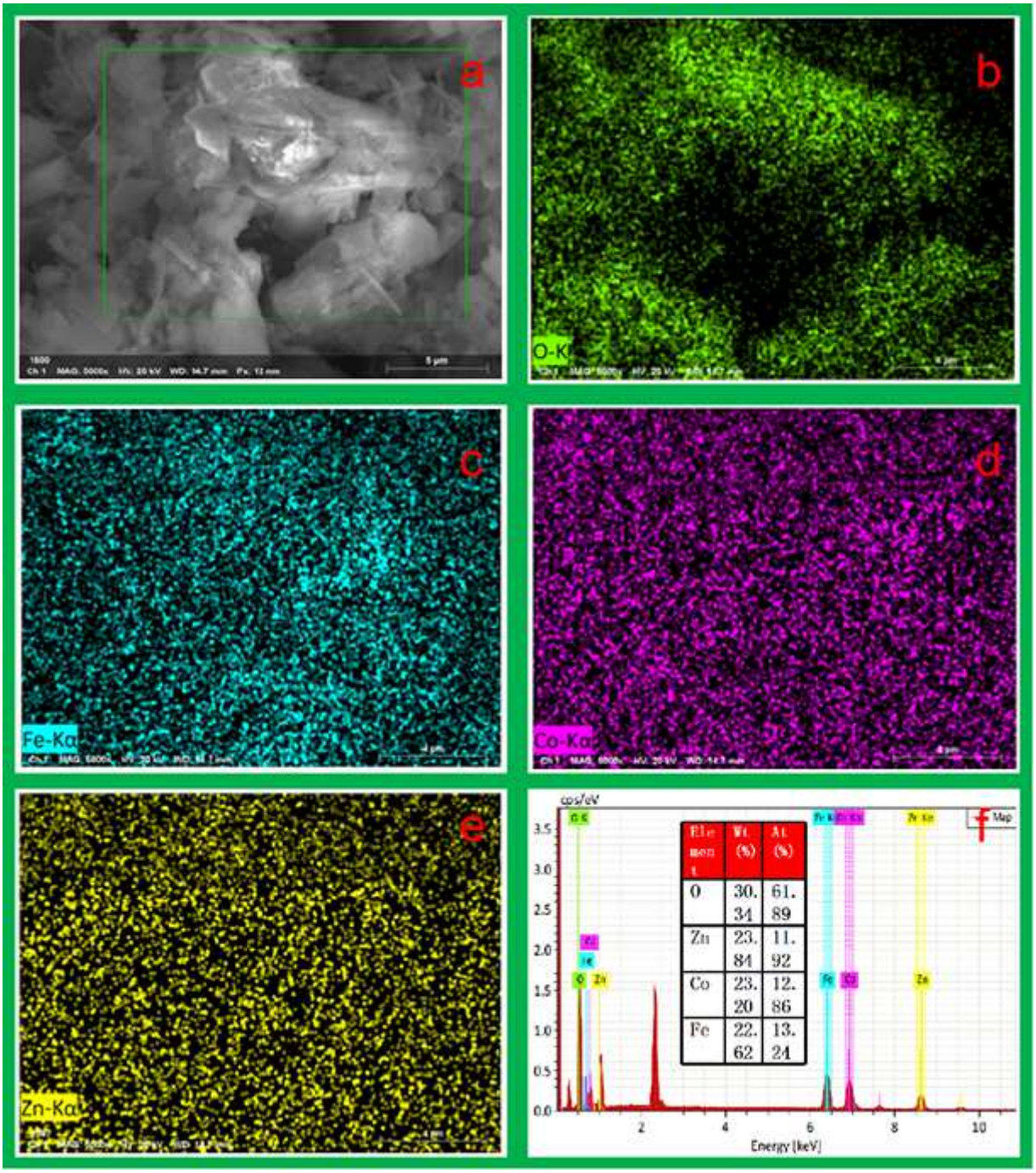

Figure 17

EDS element mapping area (a); EDS elemental mapping of O (b), Fe (c), Co (d), Zn (e); Energydiapersive X-ray spectroscopy (EDS) patterns of CoZnFeO4 (f).

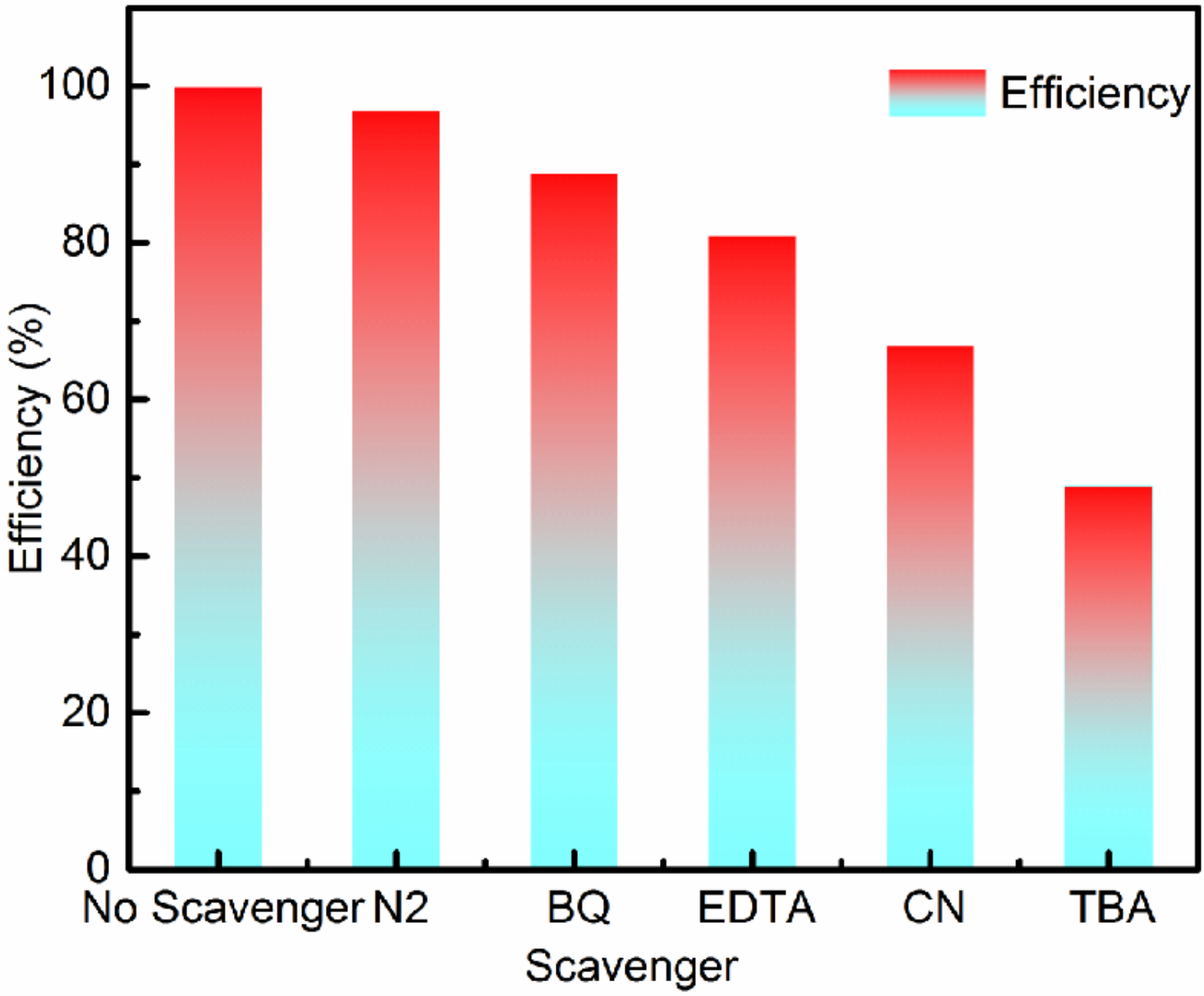

Figure 18

PhotoDecolorization of MB by Nano-CoZnFeO4 in the presence of different scavengers.

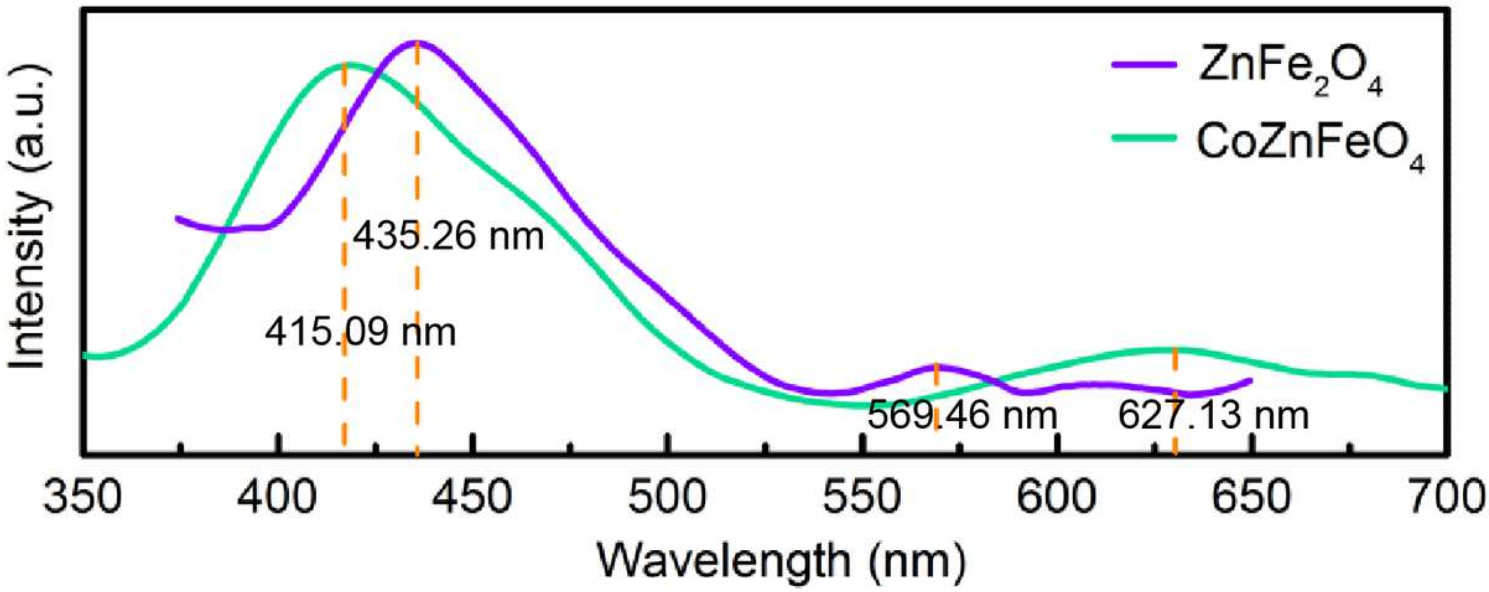

Figure 19

The PL spectra of the CoZnFeO4.

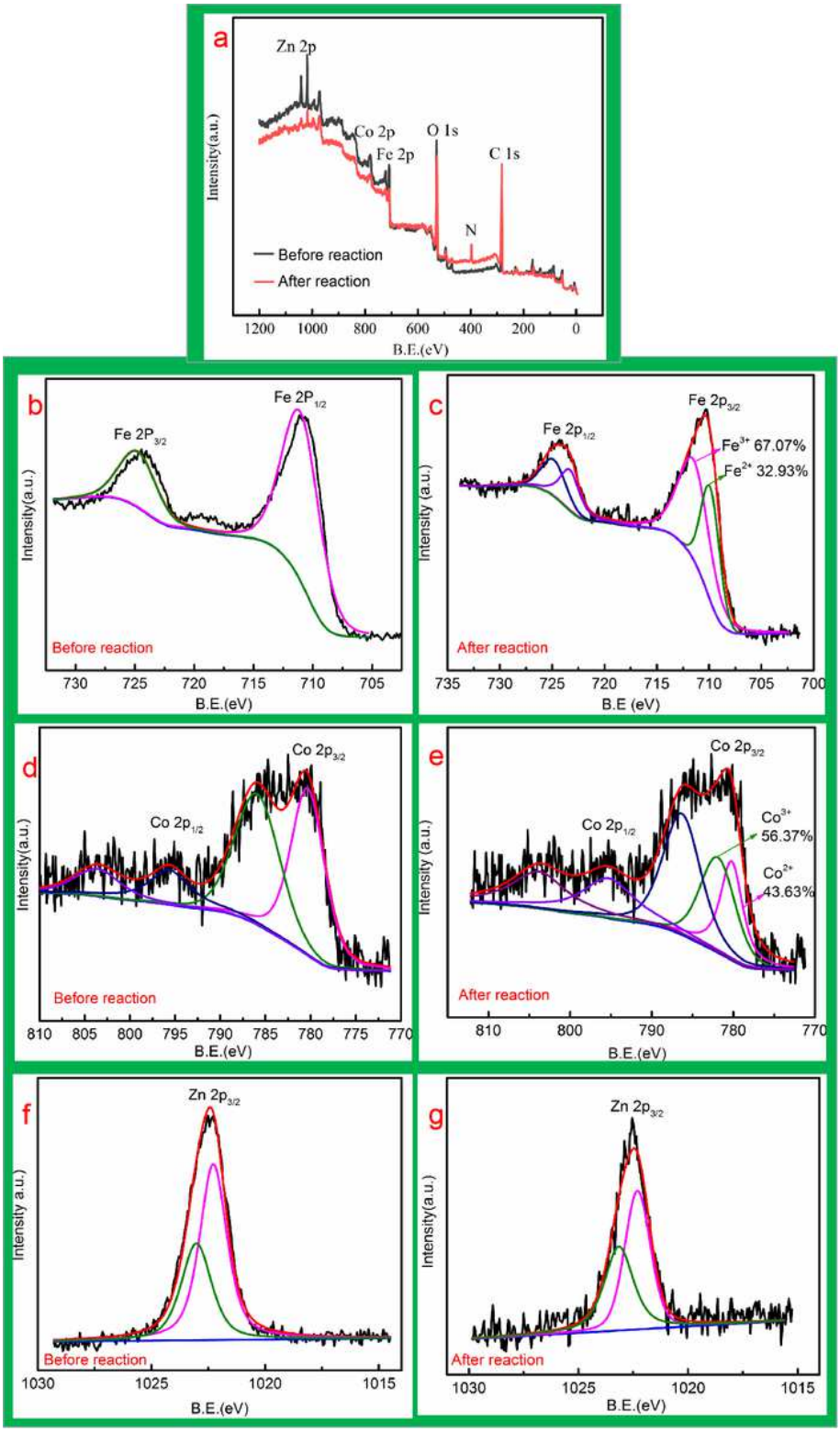

Figure 20

The XPS spectra of (a) wide-scan, (b) Co 2p (c) Fe 2p (d) O 1s of copper magnesium ferrite nanoparticles.

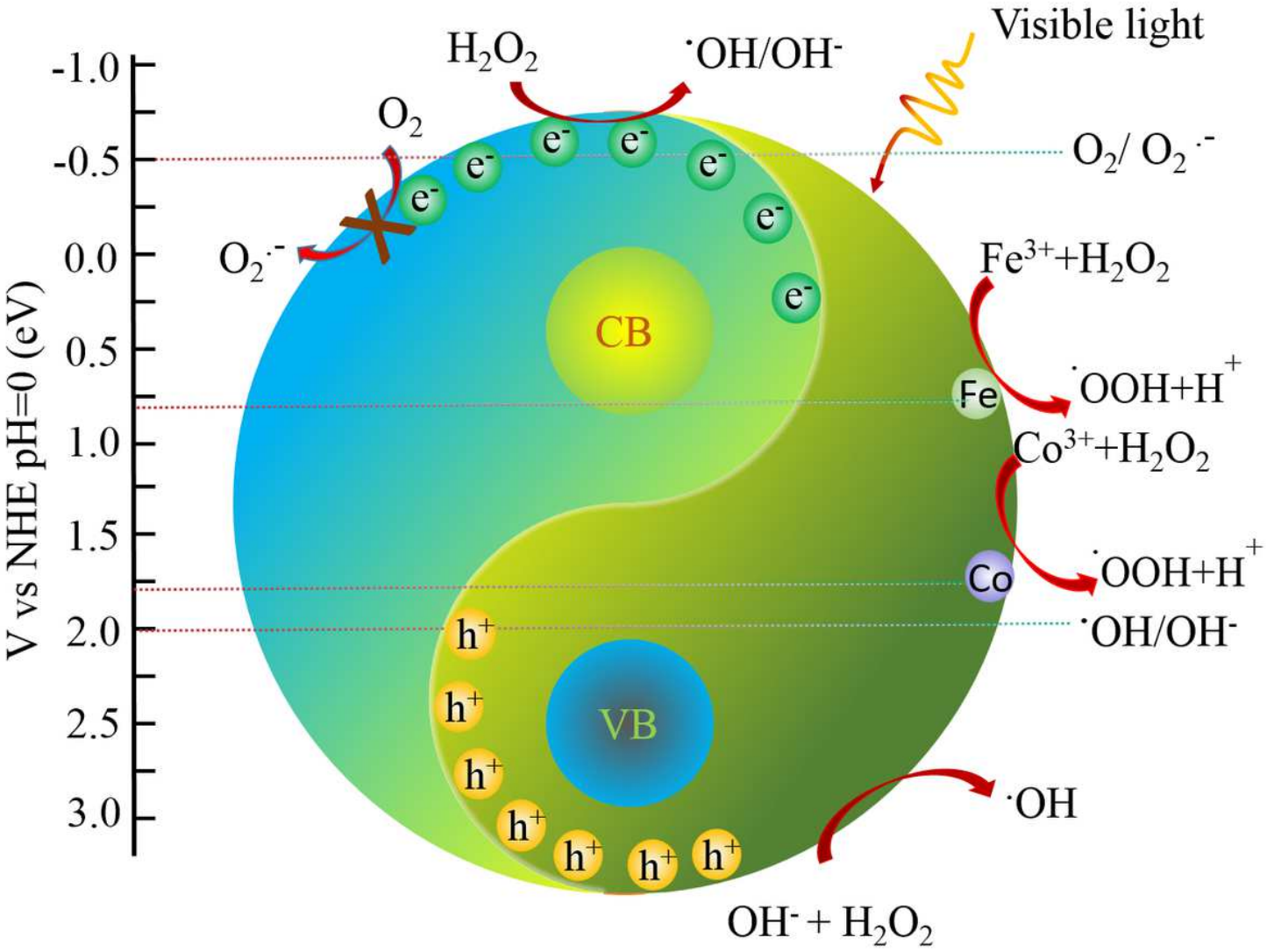

Figure 21

Schematic diagram of the degradation mechanism of CoZnFeO4

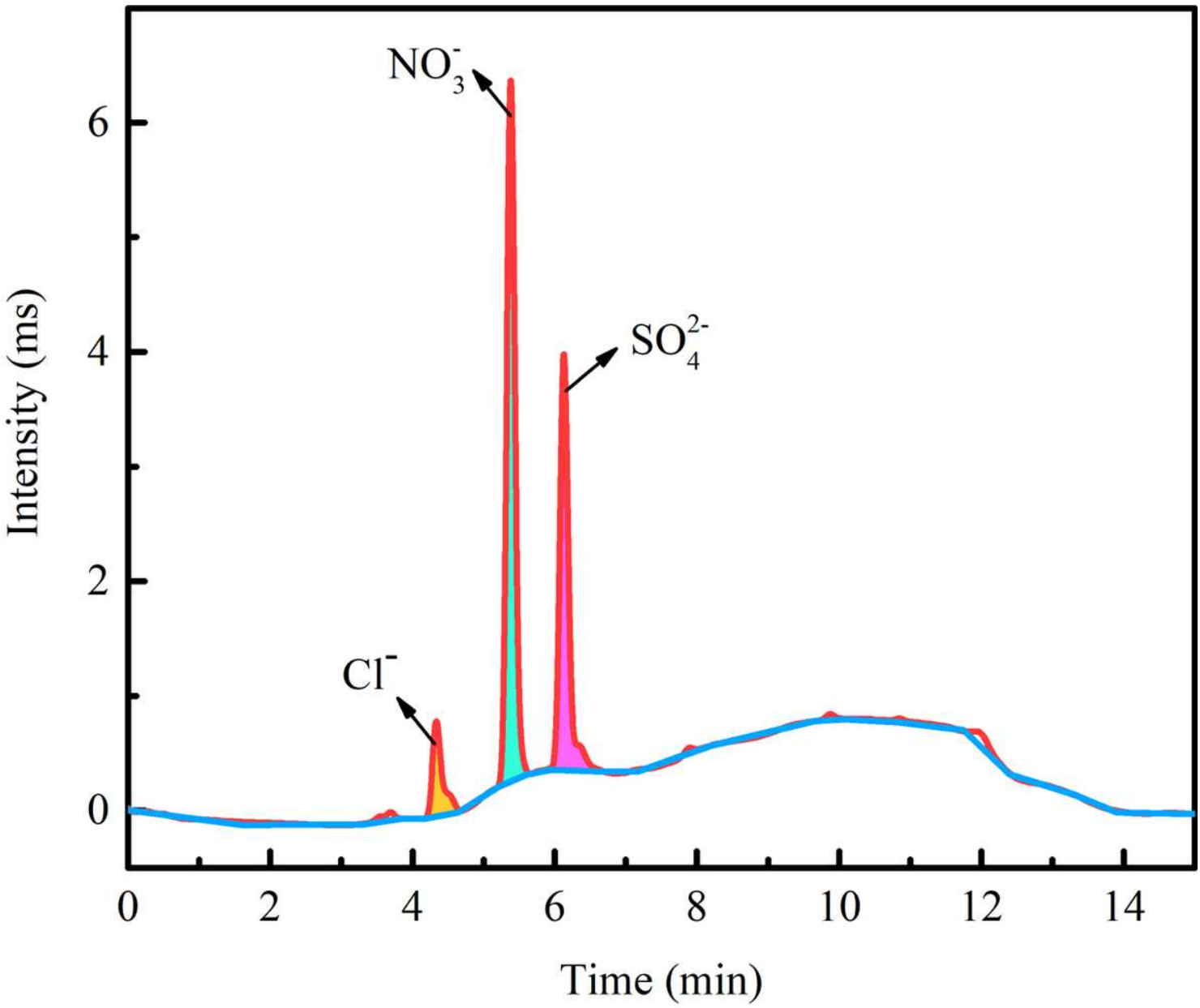

Figure 22

Ion chromatogram of reaction for 25min.

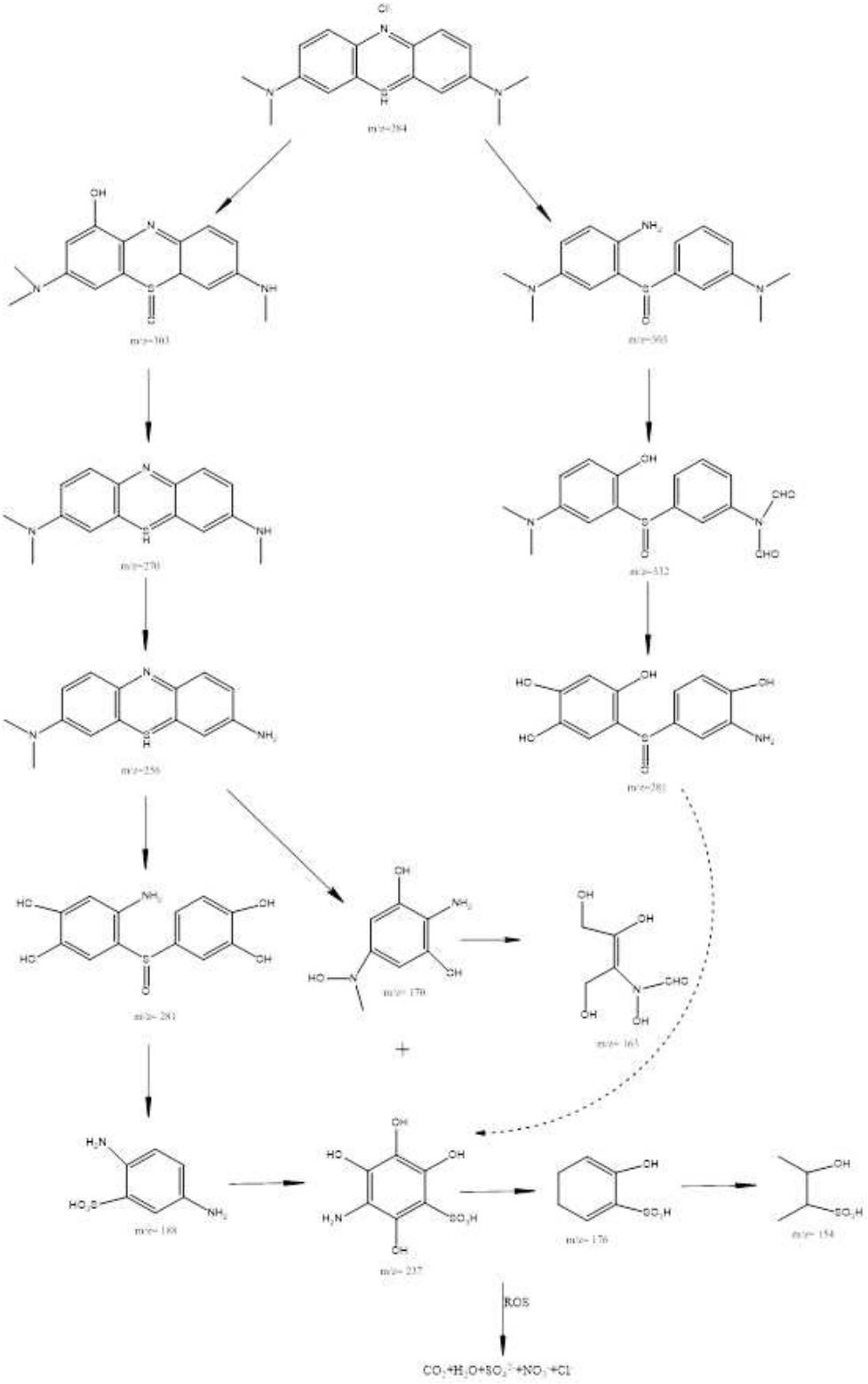

Figure 23

Methylene blue degradation pathway.

Supplementary Files

This is a list of supplementary files associated with this preprint. Click to download.

- Supportinginformation.pdf